

Heavy axion-like particles and core-collapse supernovae: constraints and impact on the explosion mechanism

Giuseppe Lucente,^a Pierluca Carenza,^{a,b} Tobias Fischer,^c Maurizio Giannotti,^d Alessandro Mirizzi^{a,b}

^aDipartimento Interateneo di Fisica “Michelangelo Merlin”, Via Amendola 173, 70126 Bari, Italy

^bIstituto Nazionale di Fisica Nucleare - Sezione di Bari, Via Orabona 4, 70126 Bari, Italy

^cInstitute for Theoretical Physics, University of Wrocław, Pl. M. Borna 9, 50-204 Wrocław, Poland

^dPhysical Sciences, Barry University, 11300 NE 2nd Ave., Miami Shores, FL 33161, USA

E-mail: g.lucente5@studenti.uniba.it, pierluca.carenza@ba.infn.it,
tobias.fischer@ift.uni.wroc.pl, MGiannotti@barry.edu,
alessandro.mirizzi@ba.infn.it

Abstract. Heavy axion-like particles (ALPs), with masses $m_a \gtrsim 100$ keV, coupled with photons, would be copiously produced in a supernova (SN) core via Primakoff process and photon coalescence. Using a state-of-the-art SN model, we revisit the energy-loss SN 1987A bounds on axion-photon coupling. Moreover, we point out that heavy ALPs with masses $m_a \gtrsim 100$ MeV and axion-photon coupling $g_{a\gamma} \gtrsim 4 \times 10^{-9}$ GeV⁻¹ would decay into photons behind the shock-wave producing a possible enhancement in the energy deposition that would boost the SN shock revival.

Contents

1	Introduction	1
2	Input of our calculation	2
2.1	SN reference model	2
2.2	Effective proton mass and chemical potential	3
2.3	Neutrino opacity	5
2.4	The characteristic radii	6
3	ALP emissivity in a supernova	8
3.1	Primakoff process	8
3.2	Photon coalescence	10
4	SN 1987A ALP bounds	11
4.1	Modified luminosity criterion	11
4.2	Free-streaming regime	14
4.3	Gravitational trapping	14
4.4	Trapping regime	16
5	Shock revival and ALP energy deposition	17
6	Conclusions	21
A	Trapping regime: the opacity criterion	23
B	Effect of the progenitor mass on the bound	27

1 Introduction

Axion-like-particles (ALPs) with masses m_a in the keV-MeV range emerge in different extension of the Standard Model, as Pseudo-Goldstone bosons of some broken global symmetry (see e.g. Sec. 6.7 of Ref. [1] for a recent review). Besides QCD axions, heavy ALPs emerge in compactification scenarios of string theory [2–4], or in the context of “relaxion” models [5]. Heavy ALPs have also recently received considerable attention in the context of Dark Matter model-building. Indeed, they may act as mediators for the interactions between the Dark Sector and Standard Model (SM) allowing to reproduce the correct Dark Matter relic abundance via thermal freeze-out [6, 7]. ALPs with masses below the MeV scale can have a wide range of implications for cosmology and astrophysics (see [8] for a review), affecting for example the Big Bang Nucleosynthesis (BBN), the Cosmic Microwave Background (CMB) [9–11] and the evolution of stars [12]. Colliders and beam-dump experiments are also capable to explore this mass range, indeed reaching the $m_a \sim \mathcal{O}(\text{GeV})$ frontier, which is not covered by any astrophysical or cosmological considerations [8, 13–15].

Core-collapse supernovae (SNe) represent a valuable cosmic laboratory to probe ALPs [16–18]. In this minimal scenario, in which ALPs couple only with photons with an effective two-photons vertex $g_{a\gamma}$, their dominant emission process in SNe is constituted by the Primakoff process on free protons, $\gamma + p \rightarrow p + a$, i.e. the conversion of a photon into an ALP in

the electric field of protons in the stellar matter. Moreover, in a medium of sufficiently high density, two photons can annihilate producing an axion, in the so called “photon coalescence” or “inverse decay process”. This effect has a kinematic threshold, vanishing for $m_a < 2\omega_{\text{pl}}$, where the plasma frequency ω_{pl} is the “effective photon mass”. This process, typically neglected in previous studies, in a SN core starts to be important for $m_a \gtrsim 10$ MeV. The ALP emission from SNe has been used to obtain constraints on the photon-ALP coupling $g_{a\gamma}$ from the SN 1987A neutrino burst [8, 19, 20]. Indeed, for values of the ALP-photon coupling $10^{-9} \text{ GeV}^{-1} \lesssim g_{a\gamma} \lesssim 10^{-5} \text{ GeV}^{-1}$, ALPs would have contributed to an excessive *energy-loss* in the SN core, shortening the observed neutrino burst. Furthermore, in [21, 22] it has been shown that for coupling $g_{a\gamma} < 10^{-9} \text{ GeV}^{-1}$, in the mass range $m_a \in [1, 100]$ MeV a further constrain can be obtained from the non-observation of a gamma-ray flux from decaying ALPs, in coincidence with the SN 1987A neutrino burst.

The goal of our paper is to take a fresh look to the SN 1987A energy-loss argument on heavy ALPs, characterizing the ALP emissivity using the state-of-the-art SN simulations. Moreover, we will examine the possible impact of ALPs on the SN explosion mechanism, in scenarios in which these particles decay into photons behind the SN shock-wave, helping its revitalization. The plan of our work is as follows. In Sec. 2 we present our SN reference model. In Sec. 3 we characterize the ALP emissivity from Primakoff and photon coalescence processes. Sec. 4 presents our update of the bounds on heavy ALPs from SN 1987A. In Sec. 5 we discuss the possible impact of decaying ALPs behind the shock-wave on the SN explosion mechanism. Finally, in Sec. 6 we summarize our results and we conclude. Two Appendices follow. In Appendix A we compare the different constraining criteria in the trapping regime, while in Appendix B we show how a change in the SN progenitor mass affects the bound.

2 Input of our calculation

2.1 SN reference model

In this work, we consider as SN reference model **AGILE-BOLTZTRAN**, which is based on spherically symmetric neutrino-radiation hydrodynamics with accurate three-flavor Boltzmann neutrino transport [23, 24], including a complete set of standard weak interactions (see Table 1 in Ref. [25]). The SN simulations are launched from the $18 M_{\odot}$ progenitor from the stellar evolution calculations of Ref. [26].

Neutrino-driven explosions cannot be obtained in spherically symmetric simulations, except for low-mass progenitor stars with masses of $M \simeq 8 - 9 M_{\odot}$ (featuring O-Ne-Mg cores [27, 28] and being associated with electron-capture SN [29]). Thus enhanced neutrino heating rates have been applied here in order to trigger the SN explosion onset at a post-bounce time $t_{\text{pb}} \approx 220$ ms, following the procedure developed in Ref. [30]. Once the explosion proceeds, the standard rates are restored. This artificial tool does not affect our results since the ALP production becomes relevant on a timescale on the order of one second after the supernova explosion has been launched. As a matter of fact, the supernova evolution at $t \gtrsim \mathcal{O}(1 \text{ s})$ is moderately independent from the details of the explosion mechanism and it can be well simulated in a spherical symmetry since multidimensional phenomena play a minor role for determining the structure at the proto-neutron star (PNS) interior where our focus will be on the high-density and high-temperature domain.

For the calculation of the ALP emissivity, we are interested in the deepest SN regions. In particular, in Fig. 1 we show in the plane of radial coordinate r vs post-bounce time t_{pb} the isocontours of the temperature T (upper left panel) and the density ρ (upper right panel). At

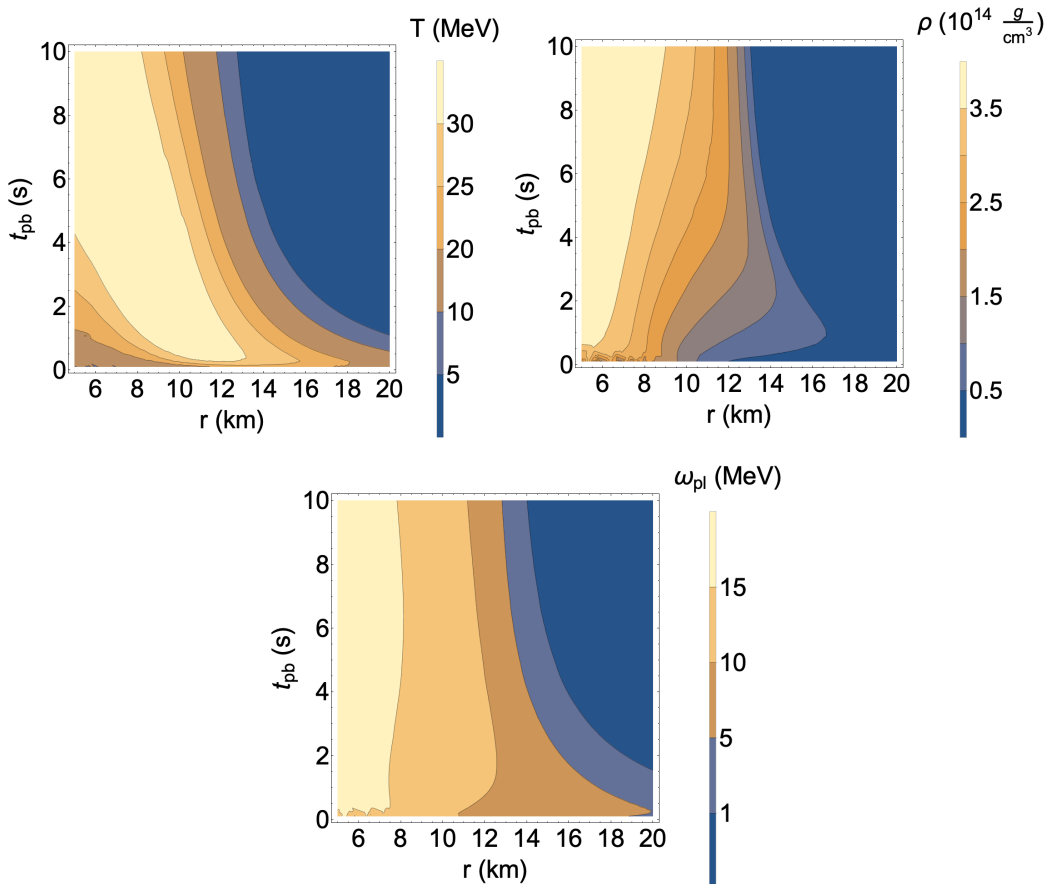


Figure 1. Isocontours of the temperature T (upper left panel), of the matter density ρ (upper right panel) and of the plasma frequency ω_{pl} (lower panel) in the plane r - t_{pb} .

early times after the core bounce ($t_{\text{pb}} \sim 1 - 3$ s), the highest temperatures [$T \sim O(40 \text{ MeV})$] are reached at $r \approx 6 - 12$ km, while at later times ($t_{\text{pb}} \sim 10$ s), the temperature is the highest at the centre and decreases at larger distances. On the other hand, due to the proto-neutron star contraction, the core density monotonically increases till it exceeds the nuclear saturation density ($\rho_{\text{sat}} \approx 2.5 \times 10^{14} \text{ g cm}^{-3}$) for $r \lesssim 10$ km. A quantity strictly dependent on the matter density ρ is the plasma frequency ω_{pl} , playing the role of an “effective photon mass”, which is an important factor in computing the photon coalescence rate. In a SN core $\omega_{\text{pl}} \simeq 16.3 \text{ MeV } Y_e^{1/3} \rho_{14}^{1/3}$ [31], where $\rho_{14} = \rho/10^{14} \text{ g cm}^{-3}$ and Y_e is the electron fraction. As shown in the lower panel of Fig. 1, at a fixed time, the plasma frequency is maximal in the inner SN core and monotonically decreases with the radius. In particular, at $t_{\text{pb}} = 1$ s, $\omega_{\text{pl}} \approx 15 \text{ MeV}$ in the interior of the proto-neutron star and it becomes smaller than 1 MeV at radii $r \gtrsim 20$ km.

2.2 Effective proton mass and chemical potential

In order to evaluate the ALP production rate, in particular the axion emission due to the Primakoff process, we have to consider two nuclear matter aspects, accounted in SN simulations: the reduction of the nuclear masses due to medium effects and the possible degeneracy of protons. Both phenomena depend on the nuclear equation of state for which the relativistic

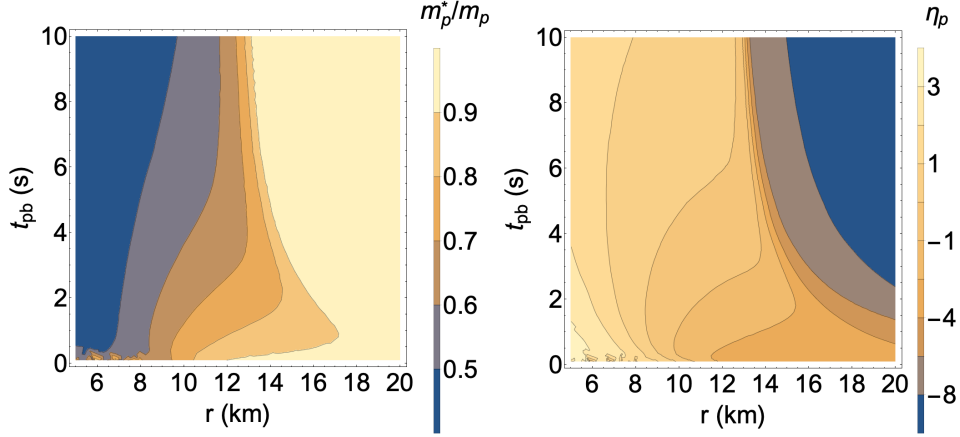


Figure 2. Isocontours of the ratio m_p^*/m_p (left panel) and of proton degeneracy parameter η_p (right panel) in the plane r - t_{pb} .

mean field model of Ref. [32] is employed here (further details can be found in Ref. [33, 34]). In particular, in the hot and dense supernova matter protons are in chemical and thermal equilibrium and obey the Fermi-Dirac statistics with the following distribution function f_p ,

$$f_p(p; \{\mu_p, T\}) = [\exp\{\beta(E(p) - \mu_p^*)\} + 1]^{-1}, \quad (2.1)$$

with inverse temperature $\beta = 1/T$ and effective chemical potential μ_p^* . Commonly used modern nuclear equations of state for supernova studies consider the strongly interacting nucleons at the mean field level [32, 33], which are based on the single-particle self energy, Σ , that can be separated into scalar (S) and the vector parts (V). This leads to the nucleon energy dispersion relation, $E(p) = \sqrt{p^2 + m_p^*}$ with the proton effective mass, $m_p^* = m_p - \Sigma_p^S$, and the definition of the effective chemical potential as follows, $\mu_p^* = \mu_p - \Sigma_p^V$, related to the proton thermodynamic chemical potential, μ_p . Note that we distinguish proton from neutron self energies here, in accordance with Ref. [33]. The difference between neutron and proton self energies is related with the nuclear symmetry energy, which has a strong density dependence [35]. In the left panel of Fig. 2 the isocontours of the ratio m_p^*/m_p in the r - t_{pb} plane are shown. We observe that at $r < 10$ km the effective proton mass is reduced by 50% with respect to its vacuum value. Indeed, the effective mass reduces steeply with increasing density above the nuclear saturation density, due to the strong density dependence of the scalar interactions in relativistic mean-field nuclear equations of state.

Note further that in our calculations of the axion emission rate, we assume non-relativistic protons and the argument in the exponent of the Fermi-Dirac distribution function becomes [34],

$$E(p) - \mu_p^* \approx m_p + \frac{p^2}{2m_p^*} + U_p - \mu_p, \quad (2.2)$$

with the definition of the proton mean-field potential, $U_p = \Sigma_p^V - \Sigma_p^S$, that allows us to rewrite the Fermi-Dirac distribution as follows,

$$f_p(p; \{\mu_p, T\}) \approx \left[\exp \left\{ \frac{p^2}{2m_p^*T} - \eta_p \right\} + 1 \right]^{-1}, \quad (2.3)$$

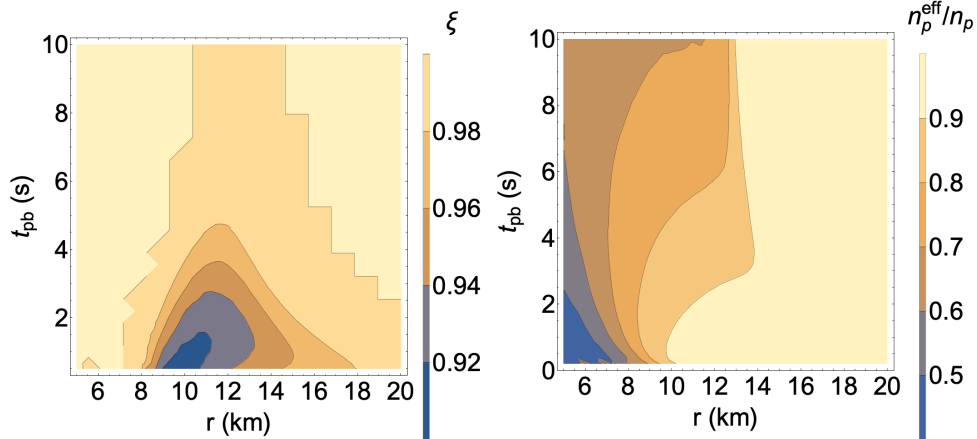


Figure 3. Isocontours of the filling factor ξ (left panel) and of the ratio n_p^{eff}/n_p (right panel) in the plane r - t_{pb} .

where we have introduced the proton degeneracy parameter, η_p , as follows,

$$\eta_p = \frac{\mu_p - m_p - U_p}{T}. \quad (2.4)$$

The right panel of Fig. 2 shows that protons are partly degenerate ($\eta_p > 1$) in the inner core of the proto-neutron star ($r < 10$ km), where the nuclear saturation density ρ_{sat} is reached.

Through the distribution function of Eq. (2.3), the free-proton number density can be obtained as

$$n_p = 2\xi \int \frac{d^3\mathbf{p}}{(2\pi)^3} f_p, \quad (2.5)$$

where 2 is the spin degeneracy factor while $\xi < 1$ is the so-called “filling factor”, which refers to unbound nuclei. It is related with the excluded volume approach of Ref. [32] employed in the nuclear equation of state to account for the dissolving of nuclear clusters with increasing density, i.e. the transition to homogeneous nuclear matter. In particular, in the limit $\xi \rightarrow 0$ all protons would be collected in clusters, while for $\xi = 1$ all protons would be free. The filling factor in our reference model is shown in the left panel of Fig. 3. As evident from the figure, this does not induce substantial corrections, since $0.9 < \xi < 1$.

Finally, the proton degeneracy implies a reduction of the number of targets $n_p \rightarrow n_p^{\text{eff}}$ for the Primakoff process. In particular, since protons are fermions the effective number of targets can be calculated by inserting the Pauli blocking factor $(1 - f_p)$ in the integral in Eq. (2.5). Thus n_p^{eff} results to be [18]

$$n_p^{\text{eff}} = 2\xi \int \frac{d^3\mathbf{p}}{(2\pi)^3} f_p (1 - f_p). \quad (2.6)$$

Contours of n_p^{eff}/n_p are shown in the right panel of Fig. 3 and indicate a suppression up to 50% in the inner core of the PNS, where the protons are degenerate.

2.3 Neutrino opacity

In order to characterize the axion emissivity in the trapping regime we need to compare the axion opacity with the neutrino one. The AGILE-BOLTZTRAN code provides a detailed

characterization of the neutrino opacity (see e.g. [36] for details). However, for the sake of the simplicity, since our treatment of the axion opacity will be simplified we prefer to use also for the neutrino case an approximated recipe. This has the benefit to allow for a semi-analytical calculation of the neutrino opacity.

In the standard scenario neutrinos are trapped in the SN core and are emitted from the last-scattering surface, the neutrino-sphere at radius R_ν . The strength of the neutrino interactions with matter is characterized through the opacity κ_ν , related to the mean-free path λ_ν by $\kappa_\nu \rho = 1/\lambda_\nu$. Since at early times the neutrino emissivity is dominated by electron species, the neutrino opacity can be roughly evaluated averaging the opacity of electron neutrinos and antineutrinos [37]

$$\kappa_\nu = \frac{L_{\nu_e} \kappa_{\nu_e} + L_{\bar{\nu}_e} \kappa_{\bar{\nu}_e}}{L_{\nu_e} + L_{\bar{\nu}_e}}, \quad (2.7)$$

where L_{ν_e} and $L_{\bar{\nu}_e}$ are the electron neutrino and antineutrino luminosities, while κ_{ν_e} and $\kappa_{\bar{\nu}_e}$ are the electron neutrino and antineutrino opacities, which have contributions from scattering κ_{sc} and absorption processes κ_{ab} . Following the derivation in [37], we define an effective opacity $\kappa_{\text{eff}} = \sqrt{\kappa_{\text{ab}}(\kappa_{\text{ab}} + \kappa_{\text{sc}})}$ with a schematic expression

$$\begin{aligned} \kappa_{\nu_e} \equiv \kappa_{\text{eff},\nu_e} &= 1.62 \frac{\sigma_0 \langle E_{\nu_e}^2 \rangle}{m_e^2} \frac{1}{m_u} X_n \sqrt{1 + 0.21 \frac{X_p}{X_n}}, \\ \kappa_{\bar{\nu}_e} \equiv \kappa_{\text{eff},\bar{\nu}_e} &= 1.62 \frac{\sigma_0 \langle E_{\bar{\nu}_e}^2 \rangle}{m_e^2} \frac{1}{m_u} X_p \sqrt{1 + 0.21 \frac{X_n}{X_p}}, \end{aligned} \quad (2.8)$$

where $m_u = 1.66 \times 10^{-24}$ g is the atomic mass unit, $m_e = 0.511$ MeV is the electron rest mass, $\sigma_0 = 1.76 \times 10^{-44}$ cm², X_p and X_n are the number fractions of free neutrons and protons.

2.4 The characteristic radii

The features of a SN explosion are strictly connected to three characteristic radii of the SN atmosphere: the neutrino-sphere radius R_ν , the gain radius R_{gain} and the shock radius R_{shock} . Note that in multi-dimensional supernova simulations, these quantities do not represent perfect spheres because of the presence of multi-dimensional phenomena such as convection and rotation induced mixing. The neutrino-sphere radius R_ν can be evaluated through the opacity κ_ν in Eq. (2.7) through the relation

$$\tau_\nu(R_\nu) = \int_{R_\nu}^{\infty} \kappa_\nu \rho dr = \frac{2}{3}, \quad (2.9)$$

where τ_ν is the optical depth. This condition corresponds to the requirement that a neutrino emerging from the neutrino-sphere has a probability $e^{-\tau_\nu} = e^{-2/3}$ to reach the infinity. For this reason, in a simplified way the proto-neutron star can be seen as a black-body cooling via neutrino emission from a surface of radius R_ν .

Actually, neutrino emission and absorption processes determine the cooling and the heating of the matter in the neutrino decoupling region, respectively. In particular, in the SN model of Fig. 1 charged-current, neutrino-nucleon/nucleus as well as neutrino-electron scattering and neutrino pair processes are considered (see Table 1 in Ref. [25], including the updates described in Refs. [25, 38]). The total heating rates Q_ν [in units of MeV cm⁻³ s⁻¹]

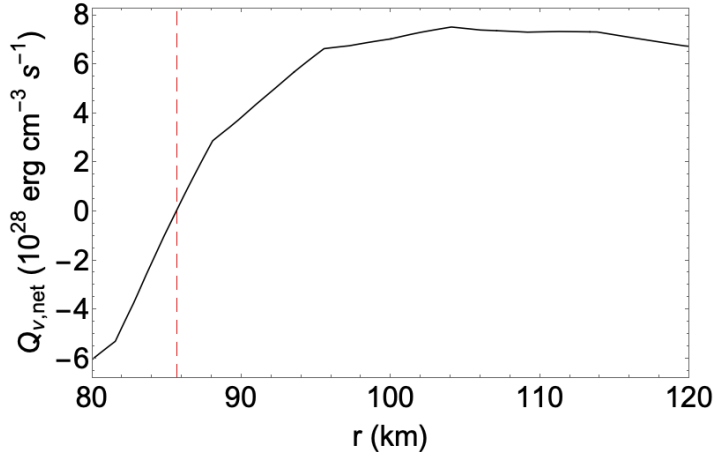


Figure 4. The net heating rate $Q_{\nu,\text{net}}$ (see text for definition) in the zone where it becomes positive at $t_{\text{pb}} = 0.3$ s. The vertical dashed red line corresponds to $R_{\text{gain}} \approx 86$ km.

are defined by the following integral expressions over the neutrino energy, E , and relative momentum angle between neutrino propagation and the radial motion, $\mu = \cos \theta$,

$$\begin{aligned}
Q_{\nu_e} = & \frac{2\pi c}{(hc)^3} \int dE E^3 \int d\mu \{ \kappa_{\nu_e}(E) f_{\nu_e}(E, \mu) - j_{\nu_e}(E)(1 - f_{\nu_e}(E, \mu)) \} \\
& + \frac{2\pi}{(hc)^3} \int dE E^2 \int d\mu \\
& \left(f_{\nu_e}(E, \mu) \frac{2\pi}{(hc)^3} \int dE' E'^2 \int d\mu' (E - E') R_{\text{scat},\nu_e}^{\text{out}}(E, E', \mu, \mu') (1 - f_{\nu_e}(E', \mu')) \right. \\
& - (1 - f_{\nu_e}(E, \mu)) \frac{2\pi}{(hc)^3} \int dE' E'^2 \int d\mu' (E - E') R_{\text{scat},\nu_e}^{\text{in}}(E, E', \mu, \mu') f_{\nu_e}(E', \mu') \\
& + f_{\nu_e}(E, \mu) \frac{2\pi}{(hc)^3} \int dE' E'^2 \int d\mu' (E + E') R_{\nu_e\bar{\nu}_e}^{\text{a}}(E, E', \mu, \mu') f_{\bar{\nu}_e}(E', \mu') \\
& \left. - (1 - f_{\nu_e}(E, \mu)) \frac{2\pi}{(hc)^3} \int dE' E'^2 \int d\mu' (E + E') R_{\nu_e\bar{\nu}_e}^{\text{p}}(E, E', \mu, \mu') (1 - f_{\bar{\nu}_e}(E', \mu')) \right)
\end{aligned} \tag{2.10}$$

of the neutrino emissivity, j_ν and opacity, κ_ν , in/out-scattering and production/absorption pair processes reaction kernels, $R_{\text{scat},\nu}^{\text{in/out}}$ and $R_{\nu\bar{\nu}}^{\text{p/a}}$, taking into account the neutrino phase space occupation in the initial, $f_\nu(E, \mu)$, and final states, $f_\nu(E', \mu')$ (further details can be found Ref. [36]). The similar expression is obtained for the $\bar{\nu}_e$ heating rate, $Q_{\bar{\nu}_e}$, as well as for the heavy-lepton flavors, $Q_{\nu_{\mu/\tau}}$ and $Q_{\bar{\nu}_{\mu/\tau}}$, except that for the latter two there is no contributions from the charged-current emissivity and opacity. The total net neutrino heating rate is then obtained by summing over all neutrino flavors, denoted as $Q_{\nu,\text{net}} = Q_{\nu_e} + Q_{\bar{\nu}_e} + 2Q_{\nu_{\mu/\tau}} + 2Q_{\bar{\nu}_{\mu/\tau}}$, where the factors of 2 arise since μ - and τ -neutrinos and antineutrinos are treated as one species. Note that contributions with a + sign belong to the total neutrino heating rate, denoted as Q_ν^+ , while those with a - sign belong to the cooling rate, denoted as Q_ν^- . It is useful to define the gain radius, R_{gain} , as the radius at which the neutrino heating balances the cooling, i.e. the net heating rate $Q_{\nu,\text{net}} \equiv Q_\nu^+ - Q_\nu^-$ vanishes, as shown in Fig. 4 for $t_{\text{pb}} = 0.3$ s. According to this definition, for $R < R_{\text{gain}}$ neutrino production prevails, $Q_\nu^+ < Q_\nu^-$, while at larger distances the absorption processes dominate.

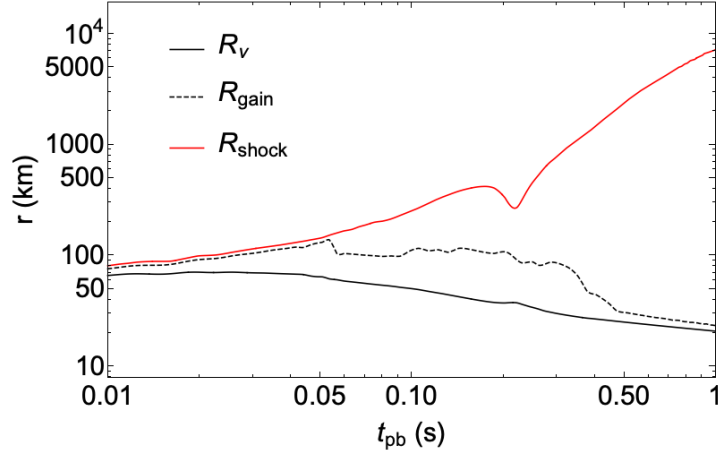


Figure 5. Time evolution of the neutrino-sphere radius R_ν (continuous black line), the gain radius R_{gain} (dashed black line) and the shock radius R_{shock} (continuous red curve).

In the so-called neutrino-driven explosion scenario, the energy deposited at early times ($t_{\text{pb}} \lesssim 0.3$ s) in the “gain layer”, i.e. the region between R_{gain} and the position of the shock-wave front R_{shock} , triggers the SN explosion. For this reason it is of crucial importance to evaluate the time evolution of the shock radius R_{shock} , beyond which the matter is not yet uncompressed.

In Fig. 5 we show the time evolution from $t_{\text{pb}} = 10$ ms to $t_{\text{pb}} = 1$ s of the three characteristic radii. We observe that the neutrino-sphere radius (the continuous black curve) is ~ 50 km at early times ($t_{\text{pb}} \lesssim 100$ ms) and it decreases to ~ 20 km at $t_{\text{pb}} = 1$ s. The gain radius R_{gain} (the dashed black curve) has a similar evolution. More specifically, $R_{\text{gain}} \sim O(100$ km) in the first 0.3 s after the core-bounce (in agreement with literature estimate [37]), but it starts decreasing all the way to $R_{\text{gain}} \approx 23$ km at $t_{\text{pb}} = 1$ s. The time evolution of the shock radius R_s is peculiar of a 1-D simulated SN explosion. It increases until $t_{\text{pb}} \approx 200$ ms but at larger times it starts receding. After the artificial enhancement of the deposited energy in the gain layer, the SN explosion is triggered and thus the shock radius begins to grow again, reaching $R_{\text{shock}} \gtrsim O(10^3$ km) at times larger than $t_{\text{pb}} \approx 0.5$ s.

3 ALP emissivity in a supernova

3.1 Primakoff process

The two-photon coupling of ALPs [39]

$$\mathcal{L}_{a\gamma\gamma} = -\frac{1}{4}g_{a\gamma}a\tilde{F}^{\mu\nu}F_{\mu\nu} , \quad (3.1)$$

allows for ALP production in a SN via the Primakoff process, i.e. the conversion of a photon into an ALP in the electric field of nuclei or electrons in the stellar matter. In the case of massive ALPs the Primakoff transition rate is given by [9, 12, 40]

$$\Gamma_{\gamma \rightarrow a} = g_{a\gamma}^2 \frac{T\kappa_s^2}{32\pi} \frac{p}{E} \left\{ \frac{\left[(k+p)^2 + \kappa_s^2 \right] \left[(k-p)^2 + \kappa_s^2 \right]}{4kp\kappa_s^2} \ln \left[\frac{(k+p)^2 + \kappa_s^2}{(k-p)^2 + \kappa_s^2} \right] - \frac{(k^2 - p^2)^2}{4kp\kappa_s^2} \ln \left[\frac{(k+p)^2}{(k-p)^2} \right] - 1 \right\} , \quad (3.2)$$

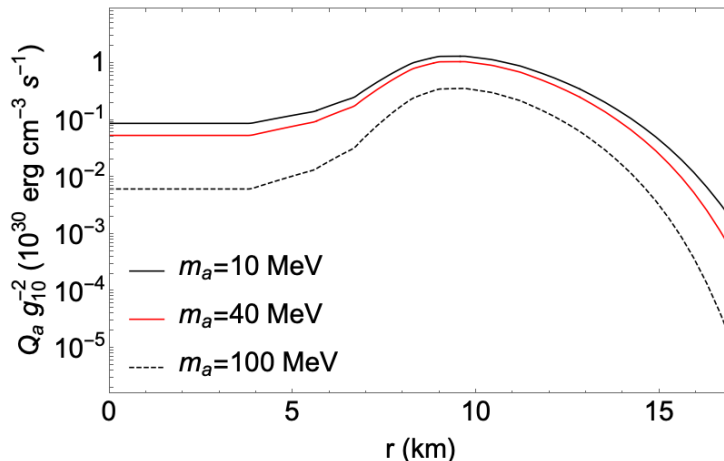


Figure 6. ALP emissivity at $t_{\text{pb}} = 1$ s for different values of the ALP mass m_a , as shown in legend.

where $p = \sqrt{E^2 - m_a^2}$ and $k = \sqrt{\omega^2 - \omega_{\text{pl}}^2}$ are the ALP and photon momentum respectively, while ω_{pl} is the plasma frequency shown in the lower panel of Fig. 1, which plays the role of an “effective photon mass”. We take $E = \omega$ since the energy is conserved. Finally, κ_s is an appropriate screening scale which accounts for the finite range of the electric field of the charged particles in the stellar medium. In a SN core, the most substantial contribution to the ALP emission via Primakoff comes from free protons. Indeed, electrons are highly degenerate in the SN core. Thus the electron phase space is Pauli-blocked and hence their contribution to the ALP production is negligible. On the other hand, protons are only partially degenerate, as shown in the right panel of Fig. 2. For this reason, only proton contribution to the Primakoff rate is considered. In the non-degenerate regime, the screening scale would be the Debye one, but in this case, in order to take into account the partial proton degeneracy, the appropriate choice for the inverse screening length is [18]

$$\kappa_s^2 = \frac{4\pi\alpha n_p^{\text{eff}}}{T}, \quad (3.3)$$

with n_p^{eff} given by Eq. (2.6). Note that a larger degeneracy implies the reduction of the effective number density of the targets and therefore the strength of the Primakoff rate is suppressed.

In order to evaluate the energy-loss by Primakoff production, one has to calculate the ALP emissivity Q_a , in units of $\text{erg cm}^{-3} \text{s}^{-1}$, which represents the energy emitted via ALP production per unit volume and time. It results

$$Q_a = 2 \int \frac{d^3\mathbf{k}}{(2\pi)^3} \Gamma_{\gamma \rightarrow a} \omega f(\omega) = \int_{m_a}^{\infty} dE E \frac{d^2 n_a}{dt dE}, \quad (3.4)$$

where the factor 2 comes from the photon polarization degrees of freedom and $f(\omega) = (e^{\omega/T} - 1)^{-1}$ is the Bose-Einstein distribution function of the thermal photons. At fixed mass m_a , the emissivity is larger at values of the radius r where the temperature T is higher. In Fig. 6 we show the ALP emissivity for different values of the ALP mass at $t_{\text{pb}} = 1$ s, normalized to the square of the ALP-photon coupling $g_{10} = g_{a\gamma}/10^{-10} \text{ GeV}^{-1}$. It is evident that, regardless of the mass m_a , the region of larger production is between $r \sim 5 - 15$ km,

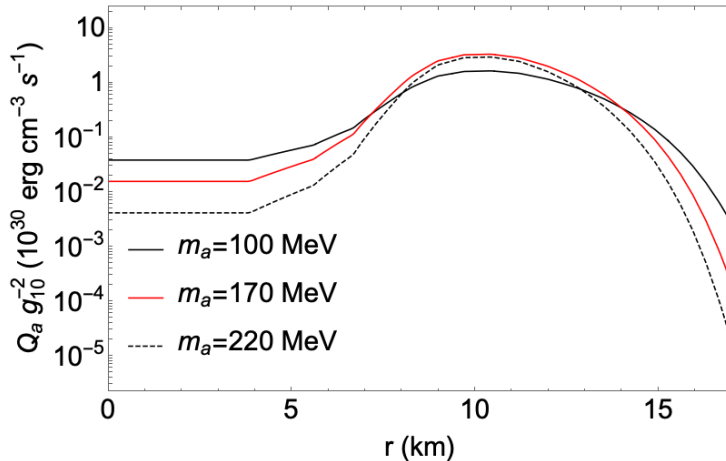


Figure 7. ALP emissivity from photon coalescence for different values of the ALP mass at $t_{\text{pb}} = 1$ s.

and the peak of the ALP emissivity is attained at $r \sim 10$ km, where the temperature reaches its maximum value, as shown in Fig. 1 (upper left panel). It is also noticeable the Boltzmann suppression of the ALP emissivity, induced by the factor $e^{-m_a/T}$, as the mass increases.

3.2 Photon coalescence

In a medium of sufficiently high density, ALPs can also be produced through the so-called “photon coalescence” or “inverse decay process” [40], where two photons can annihilate producing an axion. This process has a kinematic threshold, vanishing for $m_a < 2\omega_{\text{pl}}$.

In order to evaluate the axion production rate from photon coalescence in a thermal medium, it is convenient to approximate the Bose-Einstein photon distribution with a Maxwell-Boltzmann $f(E) \rightarrow e^{-E/T}$ for the photon occupation number [40]. The approximation is well justified since, at masses for which the coalescence process dominates, $m_a \gtrsim 100$ MeV, $E \geq m_a \gg T$. Thus, the production rate per unit volume and energy can be expressed as [12]

$$\frac{d^2 n_a}{dt dE} = g_{a\gamma}^2 \frac{m_a^4}{128\pi^3} p \left(1 - \frac{4\omega_{\text{pl}}^2}{m_a^2} \right)^{3/2} e^{-E/T}, \quad (3.5)$$

with $p = \sqrt{E^2 - m_a^2}$. The axion emissivity can be calculated as before

$$Q_a = \int_{m_a}^{\infty} dE E \frac{d^2 n_a}{dt dE}. \quad (3.6)$$

At fixed value of the axion mass m_a , the emissivity is larger at radii r where the temperature is higher because of the Boltzmann factor in Eq. (3.5). The ALP emissivities for different values of the mass m_a at $t_{\text{pb}} = 1$ s are shown in Fig. 7. Regardless of the axion mass, the emissivity is maximal at $r \approx 10$ km and the production region via photon coalescence is the same as Primakoff, between $r \approx 5 - 15$ km. As depicted in Fig. 7, in the production region the emissivity increases until $m_a \approx 170$ MeV and then it starts decreasing because of the Boltzmann suppression, while outside this region the ALP production is strongly suppressed for any mass value.

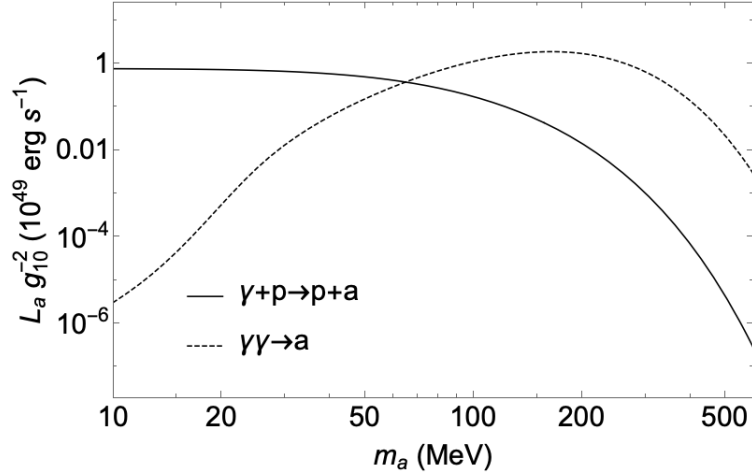


Figure 8. ALP luminosity for Primakoff (continuous curve) and photon coalescence (dashed curve) as a function of the axion mass m_a at $t_{\text{pb}} = 1$ s.

Finally, the ALP luminosity, i.e. the energy emitted per unit time (measured in erg s^{-1}), is given integrating the emissivity over the SN model, i.e.

$$L_a = 4\pi \int Q_a(r) r^2 dr. \quad (3.7)$$

In Fig. 8 the axion luminosities from Primakoff and photon coalescence as a function of the axion mass m_a at $t_{\text{pb}} = 1$ s are represented. It is apparent that the coalescence process is sub-leading for $m_a \lesssim 70$ MeV, while at larger masses it becomes dominant and reaches its maximum at $m_a \approx 170$ MeV.

4 SN 1987A ALP bounds

4.1 Modified luminosity criterion

The SN 1987A neutrino observations by KII and IMB experiments are in good agreement with the standard picture of the proto-neutron star cooling by neutrinos on a time scale of $\mathcal{O}(10 \text{ s})$ (see, e.g., [41]). If ALPs are able to transport energy out from the interior of the PNS, they would provide a new efficient cooling mechanism. Observationally, this implies that the cooling time scale would be shortened. In particular, the observed duration of the neutrino signal implies that the luminosity carried away by ALPs from the interior of the PNS to the outside of the neutrino-sphere, L_a , must not exceed the neutrino luminosity in all the six (anti)neutrino degrees of freedom L_ν in the cooling phase. This is the so-called “energy-loss argument”. Conventionally, it is taken as benchmark the neutrino luminosity value at $t_{\text{pb}} = 1$ s, $L_\nu(t_{\text{pb}} \sim 1 \text{ s}) \simeq 3 \times 10^{52} \text{ erg s}^{-1}$. Thus, the constraint on ALP emissivity is obtained requiring [42]

$$L_a(t_{\text{pb}} = 1 \text{ s}) \lesssim 3 \times 10^{52} \text{ erg s}^{-1}. \quad (4.1)$$

We stress that several numerical simulations have shown that the duration of the neutrino burst would be roughly halved when the limit (4.1) is saturated [42].

As recently proposed in [43, 44], only the ALP luminosity that cannot be reprocessed efficiently as neutrino energy is relevant to constrain the ALP parameter space. More precisely, if ALPs are produced in the zone of neutrino diffusion, i.e. behind the neutrino-sphere, energy is taken away from there. However, if they are absorbed in a region where the neutrino production is still efficient, the energy they deposit could be re-emitted via neutrino production and the neutrino signal would result to be practically unaltered. On the other hand, if ALPs reach a radius $R_{\text{far}} > R_\nu$ beyond which the neutrino production is negligible, the deposited energy would result to be essentially unavailable to them. For this reason, the axion luminosity can be evaluated by including an optical depth factor characterizing the probability that an ALP produced in the core region ($r \lesssim R_\nu$) reaches the radius R_{far} . There is a number of reasonable choices for R_{far} , the only stringent condition is that $R_{\text{far}} > R_\nu$. A lower bound on R_{far} is the neutrino gain radius R_{gain} , outside of which the neutrino production has a lower rate than the absorption one. On the other hand, a reasonable upper limit is the shock radius R_{shock} , outside of which matter is not yet uncompressed. In this work, we fix $R_{\text{far}} = R_{\text{gain}}$. From our simulation at $t_{\text{pb}} = 1$ s we find $R_{\text{gain}} \approx 23$ km, as shown in Fig. 5.

For a fixed value of R_{far} , the ALP luminosity L_a results to be [43]

$$L_a = 4\pi \int_0^{R_\nu} dr r^2 \int_{m_a}^\infty dE E \frac{d^2 n_a}{dt dE} e^{-\tau_a(r, E, R_{\text{far}})}, \quad (4.2)$$

where the volume integration is till R_ν since we are interested just in the energy taken away from behind the neutrino-sphere and the ALP volume emission rate per unit energy is given by Eq. (4.12), while $e^{-\tau_a(r, E, R_{\text{far}})}$ is the optical depth factor which takes into account the absorption effects. In particular, $\tau_a(r, E, R_{\text{far}})$, the optical depth of an ALP produced at r with energy E reaching R_{far} , results to be [43]²

$$\tau_a(r, E, R_{\text{far}}) = \left(1 - \frac{r(r - R_c)}{2R_\nu^2}\right) \int_r^{R_{\text{far}}} \frac{d\tilde{r}}{\lambda_a(E, \tilde{r})}, \quad (4.3)$$

where $R_c \approx 10$ km is the core radius and λ_a is the total axion mean free path (mfp)

$$\lambda_a^{-1} = \lambda_{a \rightarrow \gamma}^{-1} + \lambda_{a \rightarrow \gamma\gamma}^{-1}, \quad (4.4)$$

with $\lambda_{a \rightarrow \gamma}$ the inverse Primakoff mfp and $\lambda_{a \rightarrow \gamma\gamma}$ the decay mfp. In particular, the decay mfp $\lambda_{a \rightarrow \gamma\gamma}$ is

$$\lambda_{a \rightarrow \gamma\gamma} = \frac{\beta_E \gamma_E}{\Gamma_{a \rightarrow \gamma\gamma}}, \quad (4.5)$$

where $\gamma_E = E/m_a$ is the Lorentz factor, $\beta_E = \sqrt{1 - \gamma_E^{-2}}$ and $\Gamma_{a \rightarrow \gamma\gamma}$ is the decay rate

$$\Gamma_{a \rightarrow \gamma\gamma} = g_{a\gamma}^2 \frac{m_a^3}{64\pi} \left(1 - \frac{4\omega_{\text{pl}}^2}{m_a^2}\right)^{3/2}. \quad (4.6)$$

On the other hand, the inverse Primakoff mfp $\lambda_{a \rightarrow \gamma}$ results to be

$$\lambda_{a \rightarrow \gamma} = \frac{\beta_E}{\Gamma_{a \rightarrow \gamma}}, \quad (4.7)$$

²The pre-factor $\left(1 - \frac{r(r - R_c)}{2R_\nu^2}\right)$ takes into account the non-radial trajectories, but it does not deviate substantially from one [43].

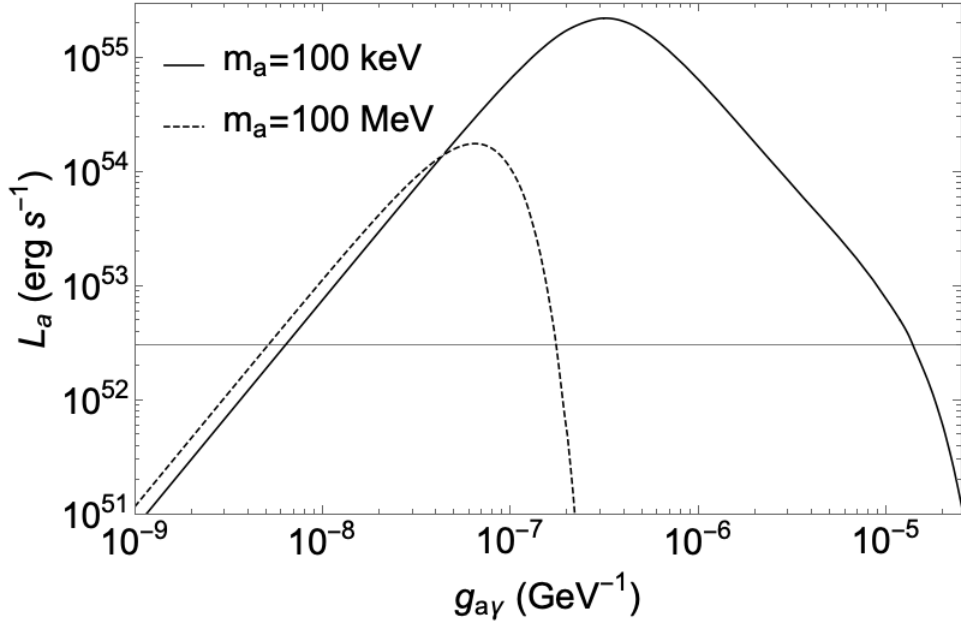


Figure 9. ALP luminosity in Eq. (4.9) as a function of the coupling constant $g_{a\gamma}$ for $m_a = 100$ keV (continuous black curve) and $m_a = 100$ MeV (dashed black curve), evaluated at $t_{\text{pb}} = 1$ s with $R_{\text{far}} = R_{\text{gain}} \approx 23$ km. The horizontal continuous black line is the critical value $L_\nu = 3 \times 10^{52}$ erg s $^{-1}$.

where $\Gamma_{a \rightarrow \gamma} = (2\beta_\gamma/\beta_E)\Gamma_{\gamma \rightarrow a}$ is the inverse Primakoff rate, with $\Gamma_{\gamma \rightarrow a}$ given by Eq. (3.2), and the factor 2 accounting for the photon polarization.

Since the integration over the energy in Eq. (4.2) influences the optical depth τ_a , for computational reasons we decided to define a mean optical depth τ_a^*

$$\tau_a^*(r, R_{\text{far}}) \equiv \tau_a(r, \langle E_a \rangle, R_{\text{far}}) \quad (4.8)$$

where $\langle E_a \rangle$ is the average axion energy over the emission spectrum.

Therefore the luminosity can be rewritten as

$$L_a = 4\pi \int_0^{R_\nu} dr r^2 e^{-\tau_a^*(r, R_{\text{far}})} \int_{m_a}^\infty dE E \frac{d^2 n_a}{dt dE} \equiv 4\pi \int_0^{R_\nu} dr r^2 Q_a(r) e^{-\tau_a^*(r, R_{\text{far}})}, \quad (4.9)$$

which is exactly the same expression in Eq. (3.7) modified with the inclusion of the optical depth factor $e^{-\tau_a^*}$. Thus the luminosity is essentially determined by the product of two factors: the emissivity Q_a , taking into account the axion production processes, and the optical depth factor $e^{-\tau_a^*}$, representing the axion absorption processes. Since both Q_a and τ_a increases as $g_{a\gamma}^2$, the luminosity L_a depends on the coupling constant $g_{a\gamma}$ as $L_a \sim g_{a\gamma}^2 e^{-g_{a\gamma}^2}$. For this reason at fixed value of the axion mass m_a , there are two critical values of the coupling $g_{a\gamma}$: $g_{a\gamma}^L$ and $g_{a\gamma}^H$, where the superscripts “L” and “H” stand respectively for “low” and “high”. For $g_{a\gamma} < g_{a\gamma}^L$, ALPs are so weakly coupled that they cannot be produced readily enough to affect the evolution of the PNS. On the other hand, for $g_{a\gamma} > g_{a\gamma}^H$ ALPs are trapped before they reach R_{far} , allowing the deposited energy to be efficiently reconverted in the form of thermal neutrinos. As shown in Fig. 9, for all the values in the range $g_{a\gamma}^L \leq g_{a\gamma} \leq g_{a\gamma}^H$ the axion luminosity L_a violates the bound $L_a \lesssim L_\nu$ and thus these values must be excluded.

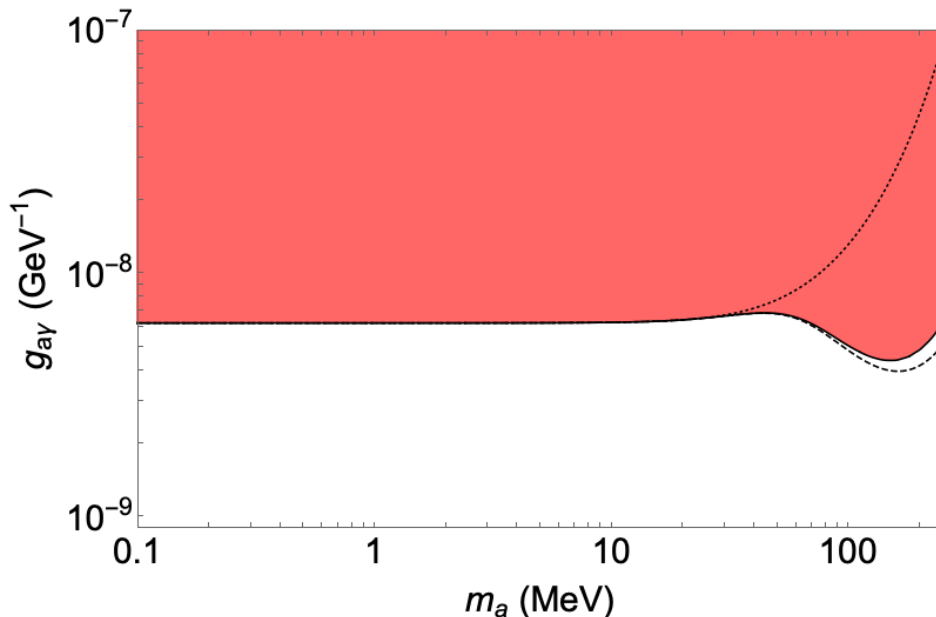


Figure 10. ALP exclusion plot in the $g_{a\gamma} - m_a$ plane coming from the energy-loss argument. The dotted black curve represents the bound accounting the ALP emissivity by only Primakoff process while the dashed black curve includes also the photon coalescence process. The continuous black curve includes the gravitational trapping effect, which is ignored in the other curves. The red region is excluded by the energy-loss argument in the free-streaming regime by accounting for the gravitational trapping.

4.2 Free-streaming regime

In the small coupling limit [$g_{a\gamma} \lesssim O(10^{-8} \text{ GeV}^{-1})$], the optical depth $\tau_a^*(r, R_{\text{far}}) \ll 1$ and thus $e^{-\tau_a^*(r, R_{\text{far}})} \sim 1$. Physically, this means that the axion mfp is significantly larger than the scale of the PNS, therefore ALPs can free stream as soon as they are produced in the SN core, leading to volume emission. In this context, the expression for the axion luminosity L_a reduces to Eq. (3.7). Imposing that L_a satisfies Eq. (4.1), one gets a constraint on the ALP-photon coupling $g_{a\gamma}$ as a function of the ALP mass m_a . Our result is shown in the exclusion plot reported in Fig. 10, in which the dotted line represents the bound obtained assuming only the Primakoff process, while the dashed curve takes into account both the Primakoff and the photon coalescence contributions. In the low-mass limit ($m_a \lesssim$ a few MeV), where the photon coalescence is not relevant, values of the ALP-photon coupling $g_{a\gamma} \gtrsim 6 \times 10^{-9} \text{ GeV}^{-1}$ are excluded, in agreement with previous results [20]. A comparison between the dotted curve and the dashed one reveals that for masses above a few 10 MeV the photon coalescence is no longer negligible. Indeed, including this channel the bound is strengthened by a factor $\gtrsim 3$ for $m_a \gtrsim 100 \text{ MeV}$ and by over an order of magnitude for $m_a \gtrsim 200 \text{ MeV}$. We note that for masses $m_a \gtrsim 170 \text{ MeV}$ the bound is weakened since the ALP production is Boltzmann-suppressed.

4.3 Gravitational trapping

ALPs produced with a kinetic energy satisfying

$$E_{\text{kin}} \leq K_{\text{tr}} \equiv \frac{G_{\text{N}} M_r m_a}{r}, \quad (4.10)$$

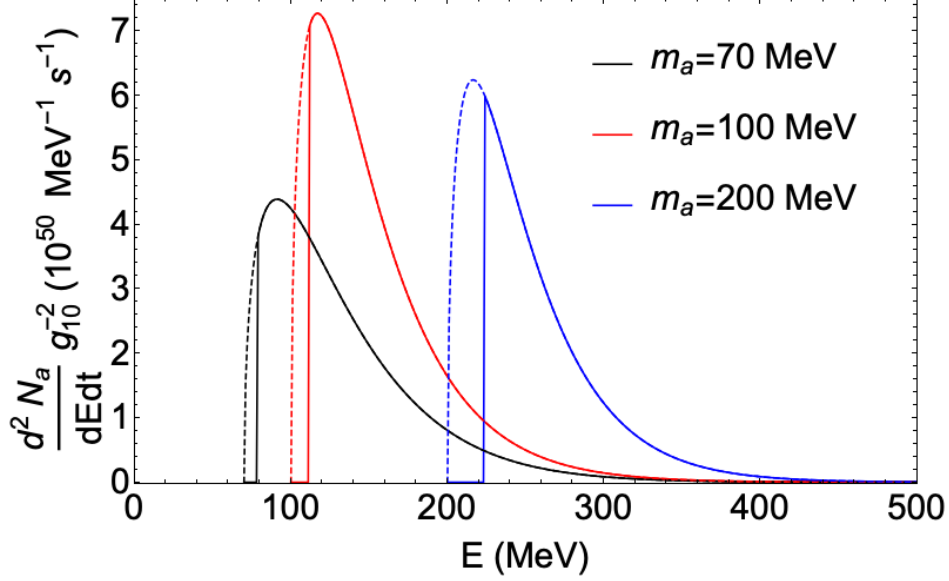


Figure 11. Total ALP production rate per unit energy at $t_{\text{pb}} = 1$ s for $m_a = 70$ MeV (black curves), $m_a = 100$ MeV (red curves) and $m_a = 200$ MeV (blue curves). The dashed curves refer to cases without the inclusion of the gravitational trapping effect, which is accounted for in the continuous curves.

will not free stream, since they are trapped by gravitational attraction [45]. In Eq. (4.10), G_{N} is the Newton constant, r is the radius at which the ALP is produced and M_r is the mass of supernova enclosed within the radius r . One can schematically include this effect by modifying the ALP volume emission rate per unit energy as

$$\frac{d^2 n_a}{dE dt} \rightarrow \frac{d^2 n_a}{dE dt} \theta(E - m_a - K_{\text{tr}}). \quad (4.11)$$

At $t_{\text{pb}} = 1$ s, the gravitational potential $U_G(r) = \frac{G_{\text{N}} M_r}{r}$ has a maximum at $r_{\text{max}} \simeq 17$ km, where $U_G(r_{\text{max}}) = U_{\text{max}} \simeq 0.12$. Therefore ALPs produced at $r \leq r_{\text{max}}$ must have a kinetic energy $E_{\text{kin}} > m_a U_{\text{max}}$ in order to escape from the potential well, otherwise they will be gravitationally trapped. For this reason the effect of the gravitational trapping is accounted in the ALP emissivity as

$$\frac{d^2 n_{a,\text{tr}}}{dE dt} = \begin{cases} \frac{d^2 n_a}{dE dt} \theta(E - m_a - m_a U_{\text{max}}) & \text{if } r \leq r_{\text{max}} \text{ ,} \\ \frac{d^2 n_a}{dE dt} \theta(E - m_a - K_{\text{tr}}) & \text{if } r > r_{\text{max}} \text{ .} \end{cases} \quad (4.12)$$

With this prescription we can compute the emissivity Q_a in Eq. (3.4) and the luminosity L_a in Eq. (4.9). We stress that, since at $t_{\text{pb}} = 1$ s the ALP production region is in the region $r \in [5; 15]$ km, essentially all the ALPs must satisfy the condition in the first line of Eq. (4.12). This implies that at fixed mass m_a , the total ALP emission rate per unit energy would be cut for $E_a \lesssim 1.12 m_a$ because of the gravitational attraction, as shown in Fig. 11. It is evident that this effect becomes more important as the ALP mass m_a increases, thus the energy-loss bound results to be relaxed at larger masses, as depicted in Fig. 10. In particular,

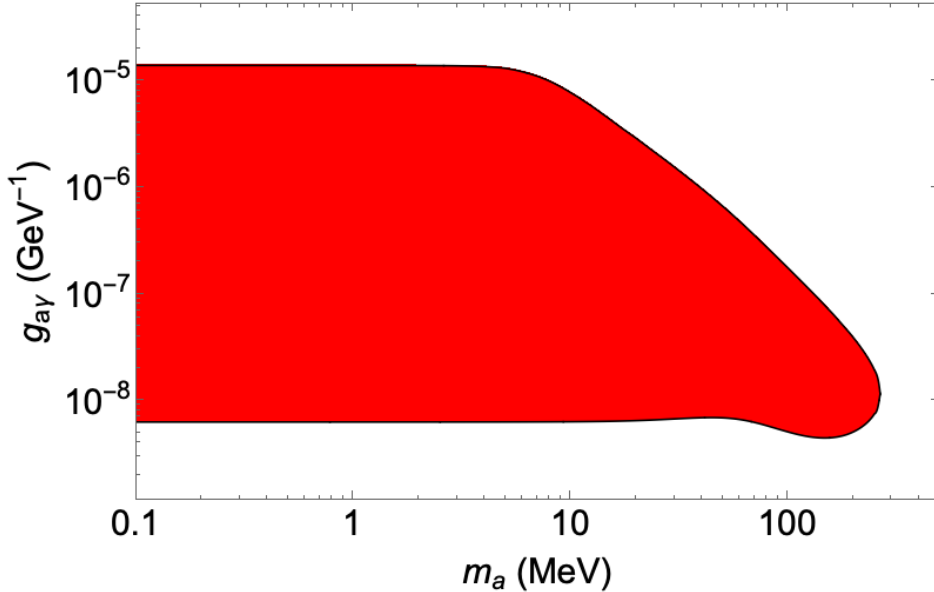


Figure 12. ALP exclusion plot in the $g_{a\gamma} - m_a$ plane obtained through the modified luminosity criterion.

for $m_a \lesssim 100$ MeV the gravitational trapping is negligible, while the bound is relaxed by $\gtrsim 15\%$ for $m_a \gtrsim 200$ MeV.

4.4 Trapping regime

As the ALP-photon coupling $g_{a\gamma}$ increases, ALPs produced in the SN core interact so strongly that their mean free path becomes smaller than the size of the SN core ($R_c \sim 10$ km). In this context, the most ALPs produced within the neutrino-sphere do not actually escape but they are reabsorbed: this is the so-called “trapping regime”. In this regime, the most relevant factor in Eq. (4.2) is the optical depth factor, characterizing the probability that an ALP produced within the neutrino-sphere reaches R_{gain} . The red region shown in Fig. 12 is excluded through the modified luminosity criterion Eq. (4.1). For each value of the axion mass, the lower bound $g_{a\gamma}^L$ is obtained in the free-streaming regime, while the upper bound $g_{a\gamma}^H$ in the trapping regime. It is interesting to stress that at $m_a \approx 266$ MeV the lower bound and the upper one are smoothly connected since the transition from the free-streaming to the trapping regime is naturally described by the optical depth factor itself. In the trapping regime, in the small mass limit ($m_a \lesssim 10$ MeV), values of the coupling $g_{a\gamma} \lesssim 1.38 \times 10^{-5}$ GeV^{-1} are excluded, while for larger masses the bound is relaxed.

A different strategy, based on the axion opacity, was often used in literature to constrain the ALP parameter space in the trapping regime. In this context, in the small mass limit ($m_a \lesssim 10$ MeV), where the dominant absorption process is the inverse Primakoff process, axions are supposed to be thermally emitted from the so-called axion-sphere, the analogous of the neutrino-sphere. This assumption has been critically assessed in Ref. [43], which shows that assuming a thermal spectrum underestimates the luminosity and thus leads to weaker limits. On the other hand, at larger masses the axion-sphere would not be well defined since the dominant absorption process is the ALP decay (see Appendix A for details). For these values of the mass, by imposing that the energy transferred by ALPs in the SN core must

be smaller than the one transported by neutrinos, one would obtain a bound on the ALP-photon coupling stronger than the one obtained through the modified luminosity criterion. A detailed comparison of these different criteria is performed in Appendix A.

Finally, we explored the dependence on the SN model of the bound on $g_{a\gamma}$. As shown in Appendix B, where we re-evaluate the bound using a SN model with a progenitor mass of $25.0 M_{\odot}$, a larger progenitor mass implies a larger exclusion region in the ALP parameter space due to the higher temperature in the SN core. However, independently on the progenitor mass, no SN simulation takes into account the axion feedback to the SN explosion, thus a self-consistent inclusion of ALPs in a SN simulation is necessary to have a more reliable bound on the ALP parameter space. Performing such a simulation would be a challenging task (see, e.g., Ref. [46] for a recent investigation in the context of dark photons), and demands a separated investigation.

5 Shock revival and ALP energy deposition

Due to the photo-dissociation of heavy nuclei the SN shock wave loses its strength and after $t_{\text{pb}} \sim 100$ ms it stalls and would eventually fall back on the SN core, if it is not revitalized by some energy injection. In the “neutrino-driven explosion scenario,” the shock is revived by neutrino heating aided by multidimensional hydrodynamical effects [47], ultimately leading to a SN explosion. However, in one-dimensional simulations the heating rates for neutrino reactions are artificially increased inside the heating region to trigger the explosion. Here we investigate the intriguing possibility that the ALP production in the SN core and their subsequent decay inside the mantle would heat the SN matter and increase the total energy of the envelope, helping the revival of the shock and the trigger of the explosion even in one dimensional simulations. Indeed, ALPs decaying into photons would provide a pressure gradient and an energy deposition in the region behind the shock, since photons quickly thermalize with matter. An amount of energy E_{dep} deposited in a region with mass M and temperature T would give an increase in entropy-per-mass [48]

$$\Delta s \approx \frac{E_{\text{dep}}}{TM/m_u}, \quad (5.1)$$

where m_u is the atomic mass unit. As the entropy-per-baryon increases, nuclei (partially) melt and at least some of the photo-dissociation burden on the shock would be relieved, definitely helping the trigger of the explosion.

A comparison between the neutrino heating in the gain layer and the ALP one would be an interesting starting point to assess the impact of ALPs on the explosion. In particular, if the energy deposited by ALPs in the gain layer competes with the neutrino one before the explosion is artificially triggered ($t_{\text{pb}} \lesssim 250$ ms), the contribution of the decaying ALPs would help the revival of the shock.

At each time step, we evaluate the rate of energy deposited by neutrinos in the gain layer as

$$L_{\nu, \text{gain}}(t) = 4\pi \int_{R_{\text{gain}}}^{R_{\text{shock}}} dr r^2 (Q_{\nu}^+ - Q_{\nu}^-), \quad (5.2)$$

where Q_{ν}^+ and Q_{ν}^- are respectively the heating and the cooling rate per unit volume, R_{gain} is the gain radius and R_{shock} the shock radius, described in Sec. 2.4. By integrating the rate

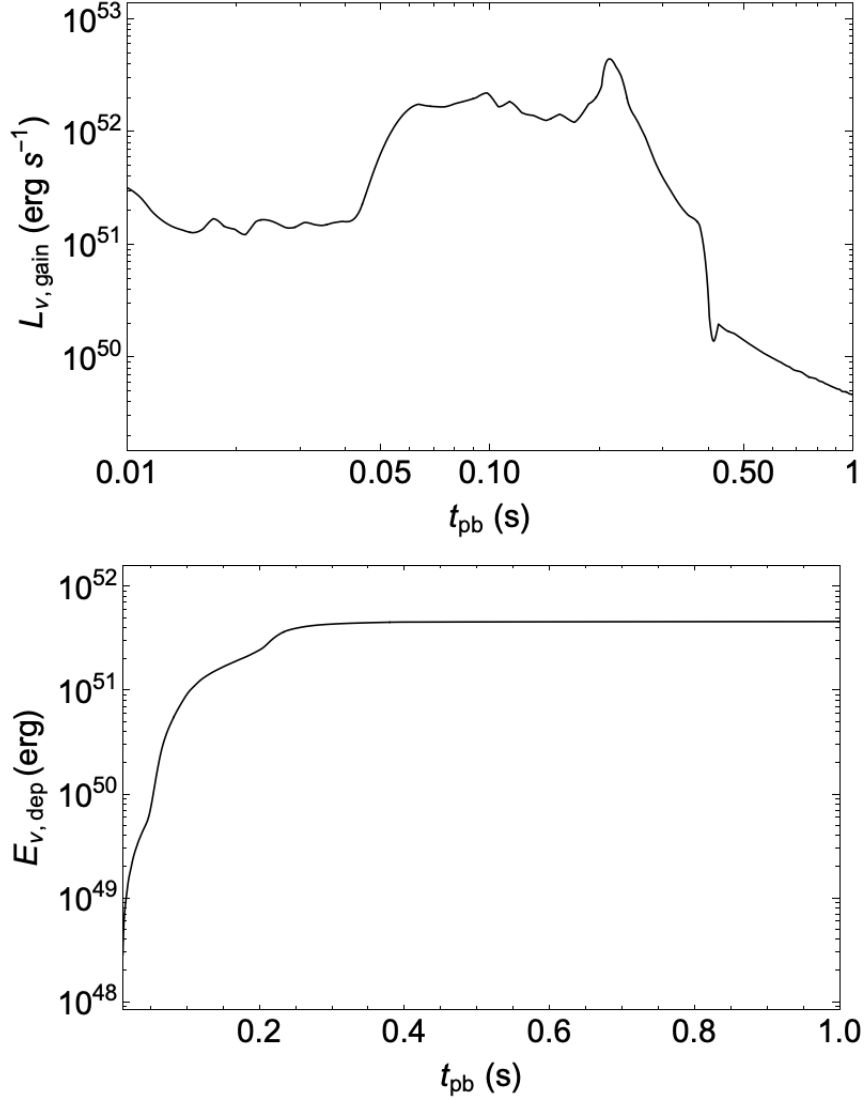


Figure 13. *Upper panel:* The neutrino energy deposition rate in the gain layer in the time-window $t_{\text{pb}} \in [10^{-2}, 1]$ s. *Lower Panel:* The energy deposited by neutrinos in the gain layer in the time-window $t_{\text{pb}} \in [10^{-2}, 1]$ s.

$L_{\nu, \text{gain}}$ over time, the energy deposition until the time t is obtained

$$E_{\nu, \text{dep}}(t) = \int_{t_0}^t d\tilde{t} L_{\nu, \text{gain}}(\tilde{t}), \quad (5.3)$$

where we fix $t_0 = 10$ ms since we are interested in the shock propagation after the neutronization burst. As shown in the upper panel of Fig. 13, the neutrino energy deposition rate is $L_{\nu, \text{gain}} \sim O(10^{51} - 10^{52} \text{ erg s}^{-1})$ for times $t_{\text{pb}} \lesssim 0.2$ s. The bump at $t_{\text{pb}} \approx 220$ ms corresponds to the artificial enhancement of the neutrino luminosity to trigger the explosion, while after the explosion has set up, $L_{\nu, \text{gain}}$ starts to decrease, becoming smaller than $O(10^{50} \text{ erg s}^{-1})$ at $t_{\text{pb}} = 1$ s. This implies that the energy deposited by neutrinos in the gain layer increases until $t_{\text{pb}} \approx 0.3$ s, saturating at $E_{\text{dep}} \approx 5 \times 10^{51} \text{ erg s}^{-1}$ for larger times, as shown in the lower

panel of Fig. 13.

In order to evaluate the ALP heating, we focus our attention on the mass range $100 \text{ MeV} \leq m_a \leq 300 \text{ MeV}$, where the dominant processes are the production via photon coalescence and the absorption via decay. At each time step, we evaluate the axion luminosity through Eq. (3.7). Assuming for the sake of simplicity that ALPs are produced at a mean radius $R_p = (\int dr r Q_a(r)) / \int dr Q_a(r)$, the rate of energy deposited at a distance R results to be

$$L_{a,\text{dep}}(t, R) = L_a(t) \left[1 - \exp \left(- \int_{R_p}^R \frac{dr}{\lambda_{a \rightarrow \gamma\gamma}(\langle E_a \rangle, r)} \right) \right], \quad (5.4)$$

with $\lambda_{a \rightarrow \gamma\gamma}$ given by Eq. (4.5) and $\langle E_a \rangle$ the average axion energy over the emission spectrum. The rate at which the ALP energy is deposited in the gain layer results to be

$$L_{a,\text{gain}}(t) = L_{a,\text{dep}}(t, R_{\text{shock}}) - L_{a,\text{dep}}(t, R_{\text{gain}}), \quad (5.5)$$

and the deposited energy is obtained by integrating over time

$$E_{a,\text{dep}} = \int_{t_0}^t dt L_{a,\text{gain}}(\tilde{t}). \quad (5.6)$$

In Fig. 14 we show the contour plot in the $g_{a\gamma} - m_a$ plane of the ALP energy deposition rate in the gain layer at different post-bounce times. At $t_{\text{pb}} = 0.1 \text{ s}$ (upper panel) the ALP energy deposition rate results to be $L_{a,\text{gain}} \sim O(10^{50} \text{ erg s}^{-1})$, two orders of magnitude smaller than the neutrino contribution at the same time. At $t_{\text{pb}} = 0.2 \text{ s}$ (middle panel) the ALP energy deposition rate in the gain layer is not negligible with respect to the neutrino one $L_{\nu,\text{gain}} \approx 2.3 \times 10^{52} \text{ erg s}^{-1}$ (the dashed black contour in the middle panel of Fig. 14 corresponds to one tenth of $L_{\nu,\text{gain}}$). Therefore, ALPs could help the trigger of the explosion for a range of parameters not excluded by the energy-loss argument, namely in the mass range $150 \text{ MeV} \lesssim m_a \lesssim 220 \text{ MeV}$ and for values of the coupling constant $g_{a\gamma} \gtrsim 4 \times 10^{-10} \text{ GeV}^{-1}$. After the explosion is triggered, the axion heating rate continues to increase and becomes much larger than the neutrino one since this latter rapidly decreases. In particular, at $t_{\text{pb}} = 0.3 \text{ s}$ (lower panel) $L_{\nu,\text{gain}} \approx 4 \times 10^{51} \text{ erg s}^{-1}$, while $L_{a,\text{gain}} \sim O(10^{52} \text{ erg s}^{-1})$.

In Fig. 15 we show the time evolution of the energy deposition rate (upper panel) and of the energy deposited by ALPs in the gain layer (lower panel) for a fixed value of the coupling constant $g_{a\gamma} = 4 \times 10^{-10} \text{ GeV}^{-1}$ and a representative value of the axion mass $m_a = 200 \text{ MeV}$ (dashed black curves). At early times ($t_{\text{pb}} < 0.2 \text{ s}$) $L_{a,\text{gain}} \ll L_{\nu,\text{gain}}$, while the ALP energy deposition rate becomes larger than $L_{\nu,\text{gain}}$ at times $t_{\text{pb}} \gtrsim 2.5 \text{ s}$. Similarly, the energy deposited by ALPs in the gain layer is negligible at times $t_{\text{pb}} \lesssim 0.2 \text{ s}$ since it is more than an order of magnitude smaller than the one deposited by neutrinos at the same time. However, the former constantly increases and becomes greater than $5 \times 10^{51} \text{ erg}$ (the saturation value of the deposited neutrino energy) at times $t_{\text{pb}} \gtrsim 0.5 \text{ s}$.

In particular, at $t_{\text{pb}} \approx 0.3 \text{ s}$, $E_{a,\text{dep}} \sim O(10^{51} \text{ erg})$, the mass of the gain layer is $M \sim O(0.1 M_\odot)$ and the temperature in this region is $T \approx 2 \text{ MeV}$. Therefore, by Eq. (5.1) one has $\Delta s \approx$ a few units of Boltzmann's constant per baryon, an increase sufficient to partially melt nuclei and help the SN explosion.

One may conclude that for axion couplings below the energy-loss bound, one can still have a non-negligible axion heating for the ALP parameters $150 \text{ MeV} \lesssim m_a \lesssim 220 \text{ MeV}$ and $g_{a\gamma} \gtrsim 4 \times 10^{-10} \text{ GeV}^{-1}$, which would help the SN explosion. In principle, one could convert the

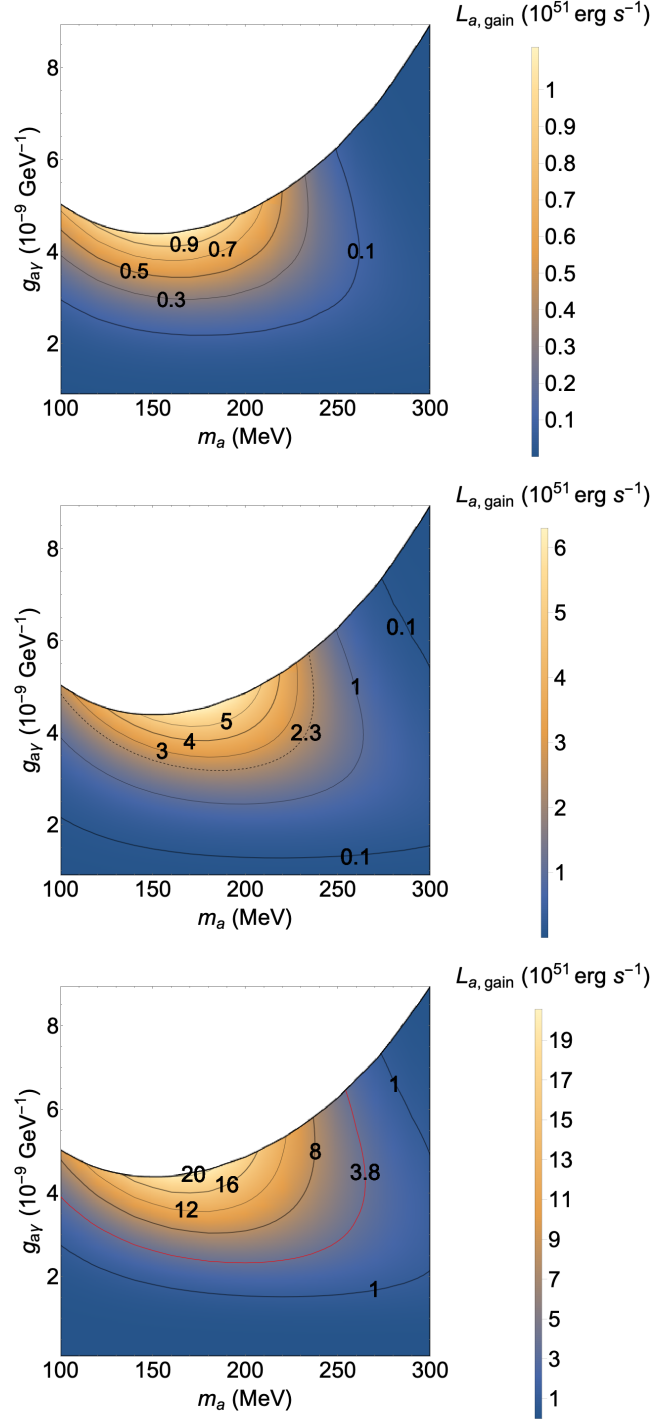


Figure 14. Isocontours in the $g_{a\gamma} - m_a$ plane of the ALP energy deposition rate in the gain layer at $t_{\text{pb}} = 0.1$ s (upper panel), $t_{\text{pb}} = 0.2$ s (middle panel), $t_{\text{pb}} = 0.3$ s (lower panel). The dashed contour in the middle panel corresponds to the one tenth of $L_{\nu,\text{gain}}$ at $t_{\text{pb}} = 0.2$ s, while the red contour in the lower panel corresponds to $L_{\nu,\text{gain}} \approx 3.8 \times 10^{51} \text{ erg s}^{-1}$ at $t_{\text{pb}} = 0.3$ s. In all the panels, the white region is excluded by the energy-loss argument.

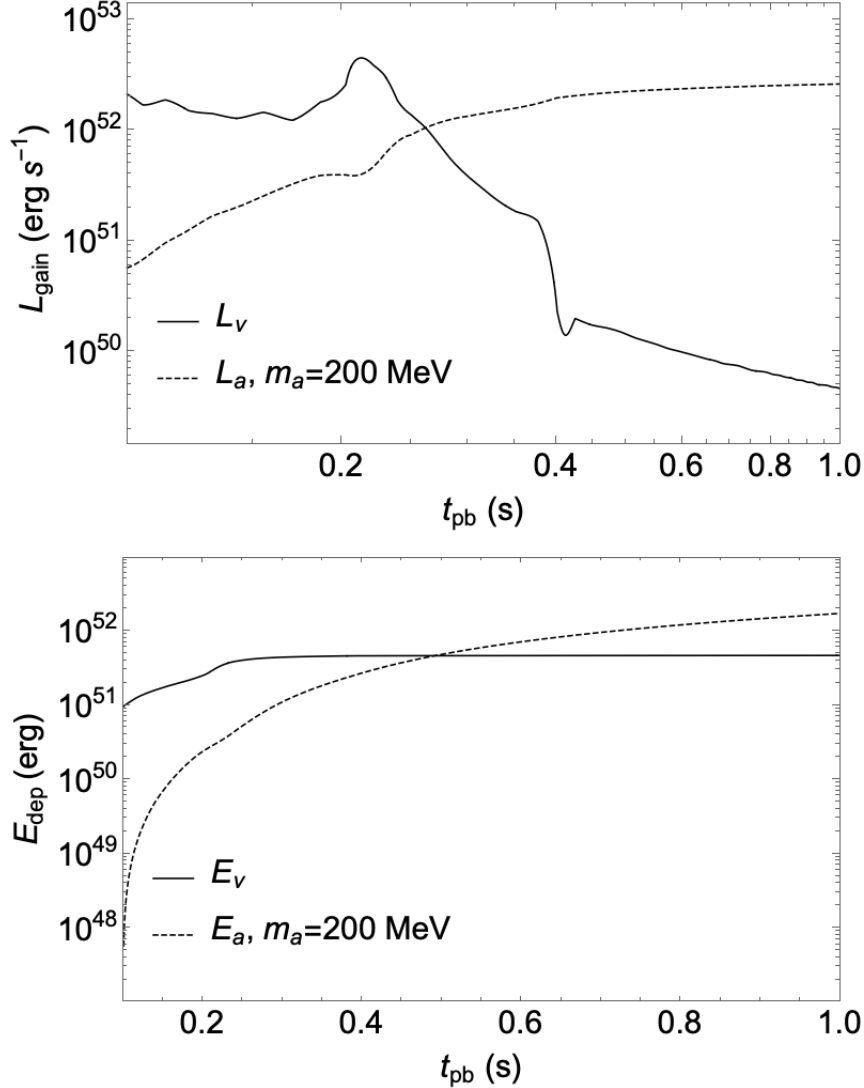


Figure 15. The time evolution of the energy deposition rate (upper panel) and of the energy deposited (lower panel) in the gain layer by neutrinos (continuous black curves) and by ALPs (dashed black curves) with mass $m_a = 200$ MeV and coupling constant $g_{a\gamma} = 4 \times 10^{-10} \text{ GeV}^{-1}$.

ALP deposited energy into an explosion energy E_{expl} [30] and constrain the ALP parameter space by imposing $E_{\text{expl}} \lesssim 3 \times 10^{51} \text{ erg}$ [49]. However, only a simulation including ALPs could provide reliable results and strengthen the validity of the hints obtained (see e.g. [50] for radiatively decaying standard axions or [51] for decaying sterile neutrinos).

6 Conclusions

In this work we used the state-of-the-art SN one-dimensional simulations to revise and update the mechanism of the emission from the SN core of heavy axion-like particles (ALPs), with masses of the order 1-100 MeV interacting with photons. In particular, we added the contribution of the photon coalescence process, neglected in previous studies, which dominates at masses $m_a \gtrsim 100$ MeV and allows one to improve the previous constraints on the

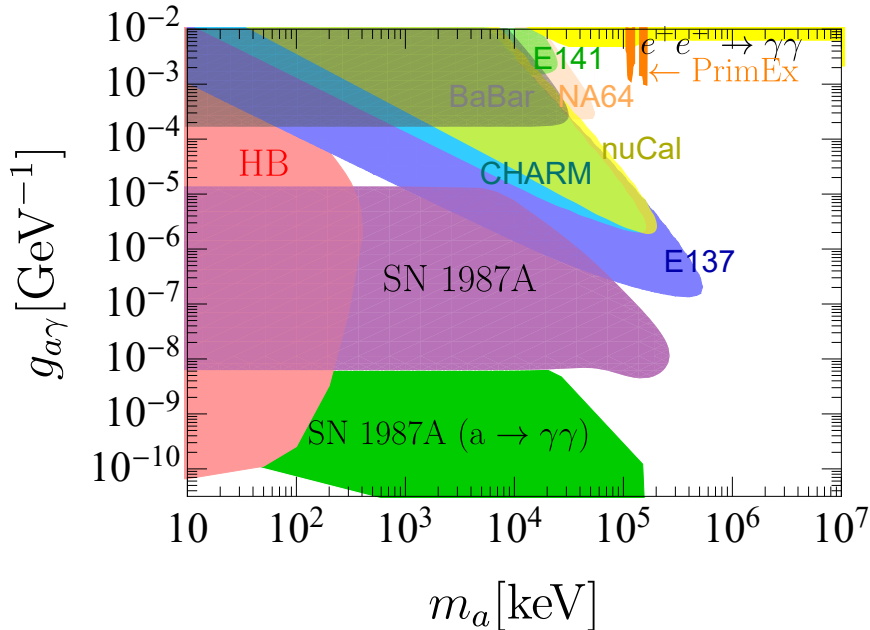


Figure 16. Overview of the heavy ALP parameter space in the plane $g_{a\gamma}$ vs m_a . The purple-filled region labelled “SN 1987A” represents our new exclusion result. The HB bound [12], the constraint from visible decays of ALPs produced in SN 1987A [22] and the experimental limits, compiled from Refs. [8, 12, 14, 15], are also shown.

ALP parameter space. The detailed analysis of the SN simulations, which provides the time evolution of the characteristic radii of the SN atmosphere, allows one to consistently apply a recently proposed method (dubbed the “modified luminosity criterion”) to explore the ALP parameter space, firstly presented in [43] and based on the assumption that only the energy which cannot be efficiently reprocessed by the neutrino fluid is relevant to constraint the ALP parameters. Through this method, in the free-streaming regime we confirm the previous bounds in the low-mass limit [$m_a \lesssim 10$ MeV] since the photon coalescence contribution is suppressed as m_a^4 , while constraints are sensitively improved at large masses. In particular, the inclusion of the photon coalescence allows us to strengthen the previous bounds in this regime by more than an order of magnitude for masses $m_a \gtrsim 200$ MeV. On the other hand, in the trapping regime values of the coupling $g_{a\gamma} \lesssim 1.4 \times 10^{-5} \text{ GeV}^{-1}$ are excluded in the small mass limit, while the bound is relaxed for larger masses. In Fig. 16 we show the updated constraints on heavy ALPs. As discussed in Appendix A, in the trapping regime the modified luminosity criterion is more reliable than the constraining criterion based on ALP opacity used in prior works. However the uncertainties related to the SN model and the difficulties to deal with trapped ALPs suggest the importance to develop a SN simulation with a self-consistent inclusion of ALPs to have an even more reliable bound on the ALP parameter space.

The early time evolution of the SN simulation allows one to assess the possible impact of the ALP production to trigger the SN explosion. In particular, following an original approach through which the neutrino heating rates and the ALP ones are compared, we endow a region of the parameter space with masses $m_a \approx 200$ MeV and coupling constant

$g_{a\gamma} \gtrsim 4 \times 10^{-9} \text{ GeV}^{-1}$ for which the ALPs decaying into photons would provide an efficient energy deposition behind the shock which could help the SN explosion. It is quite intriguing that ALPs could be identified as the yet-missing piece of the puzzle to boost the supernova explosion energy in present neutrino-driven explosion models. A further exploration of this aspect motivates the involvement of multi-dimensional supernova models.

Acknowledgments

We thank the anonymous referee for the valuable comments on our manuscript. The work of P.C. and A.M. is partially supported by the Italian Istituto Nazionale di Fisica Nucleare (INFN) through the ‘‘Theoretical Astroparticle Physics’’ project and by the research grant number 2017W4HA7S ‘‘NAT-NET: Neutrino and Astroparticle Theory Network’’ under the program PRIN 2017 funded by the Italian Ministero dell’Università e della Ricerca (MUR). T. F. acknowledges support from the Polish National Science Center (NCN) under Grant No. 2016/23/B/ST2/00720 and No. 2019/33/B/ST9/03059. The supernova simulations are performed at the Wroclaw Center for Scientific Computing and Networking (WCSS) in Wroclaw (Poland).

A Trapping regime: the opacity criterion

A different approach to constrain the ALP parameter space in the trapping regime is based on the assumption that trapped ALPs may contribute significantly to the energy transport in the star, i.e. they would remove energy from one region of the PNS and deposit it at an approximate distance of one mfp, modifying the SN evolution. In this context, one defines the ALP Rosseland mfp as $\lambda_a = (\kappa_a \rho)^{-1}$ in terms of the Rosseland opacity [52]

$$\kappa_a^{-1} = \frac{\int_{m_a}^{\infty} \kappa_E^{-1} \beta_E \partial_T B_E dE}{\int_{m_a}^{\infty} \beta_E \partial_T B_E dE}, \quad (\text{A.1})$$

where

$$B_E = \frac{1}{2\pi^2} \frac{E^2 (E^2 - m_a^2)^{1/2}}{e^{E/T} - 1} \quad (\text{A.2})$$

is the ALP thermal spectrum and the ALP opacity κ_E is evaluated by considering in Eq. (A.1) the contributions of the inverse Primakoff effect $a + p \rightarrow p + \gamma$ and the decay process $a \rightarrow \gamma\gamma$

$$\kappa_E = \kappa_{a \rightarrow \gamma} + \kappa_{a \rightarrow \gamma\gamma}. \quad (\text{A.3})$$

In particular, the decay contribution $\kappa_{a \rightarrow \gamma\gamma}$ results to be $\kappa_{a \rightarrow \gamma\gamma} \rho = \lambda_{a \rightarrow \gamma\gamma}^{-1}$, where $\lambda_{a \rightarrow \gamma\gamma}$ is the decay mfp in Eq. (4.5), while the inverse Primakoff contribution $\kappa_{a \rightarrow \gamma}$ is $\kappa_{a \rightarrow \gamma} \rho = \lambda_{a \rightarrow \gamma}^{-1}$, with $\lambda_{a \rightarrow \gamma}$ the inverse Primakoff mfp in Eq. (4.7).

When the ALP mass is less than few MeV, the inverse Primakoff process dominates over the decay, which has a strong dependence on the axion mass (m_a^3) and is forbidden for $m_a < 2\omega_{\text{pl}}$. Since the Primakoff opacity is strictly dependent on the matter density ρ , in the low-mass limit ALPs are trapped in the inner SN core and they are emitted from an ‘‘axion-sphere’’, the analogous of the ‘‘neutrino-sphere’’, with a radius R_a determined by the condition

$$\tau_a(R_a) = \int_{R_a}^{\infty} \kappa_a \rho dr = \frac{2}{3}, \quad (\text{A.4})$$

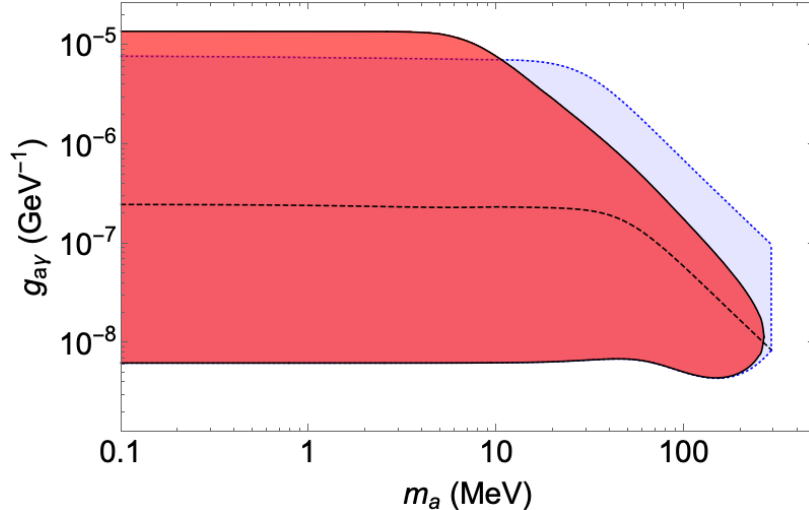


Figure 17. Exclusion plot in the plane m_a - $g_{a\gamma}$. The shaded red area is excluded by the modified luminosity criterion, while the light blue area is excluded by splitting the calculation in two different regimes (details in the text). The dashed black line represents the border between the free-streaming and trapping regimes.

where κ_a is the Rosseland mean opacity defined in Eq. (A.1). Therefore, in this approach, for masses $m_a \lesssim O(1 \text{ MeV})$, trapped ALPs are expected to have a black-body emission with a luminosity $L_a \propto R_a^2 T^4(R_a)$. The bound on the coupling $g_{a\gamma}$ is obtained by imposing [53]

$$L_a \lesssim L_\nu. \quad (\text{A.5})$$

This condition excludes the values of the photon-axion coupling $g_{a\gamma} \lesssim 7.7 \times 10^{-6} \text{ GeV}^{-1}$, in agreement with Ref. [8].

For heavier ALPs, $m_a \gtrsim 10 \text{ MeV}$, the decay process becomes dominant. This implies that at these masses the “axion-sphere” cannot be well defined because the integral in Eq. (A.4) always diverges since the decay mfp tends to a constant value in vacuum. In this context, ALPs may decay before leaving the SN core, contributing to the energy transfer. In order to constrain $g_{a\gamma}$ one should impose at the neutrino-sphere R_ν that

$$\kappa_a \gtrsim \kappa_\nu, \quad (\text{A.6})$$

where κ_ν is the neutrino opacity, given by Eqs. (2.7)–(2.8). The bound obtained following this approach has to be connected with the one for the low-mass case dominated by the Primakoff process, computed through Eq. (A.5). The resulting constraint is constant in the low-mass limit $m_a \lesssim 10 \text{ MeV}$ while for higher masses it decreases as $\sim m_a^{-3/2}$, as shown in Fig. 17, where the shaded red region is excluded through the modified luminosity criterion, while the light blue region delimited by a dotted blue line represents the region excluded by combining the energy-loss argument in the free-streaming and the energy-transfer argument in the trapping regime. A disadvantage of the approach described in this Appendix is that one has to split the calculation into two different regimes, while with the modified luminosity criterion the transition from the free-streaming to the trapping regime is smooth due to the presence of the optical depth factor. Therefore, in this case one needs a strategy to assess for which values of the ALP parameters the free-streaming approximation is good. In particular,

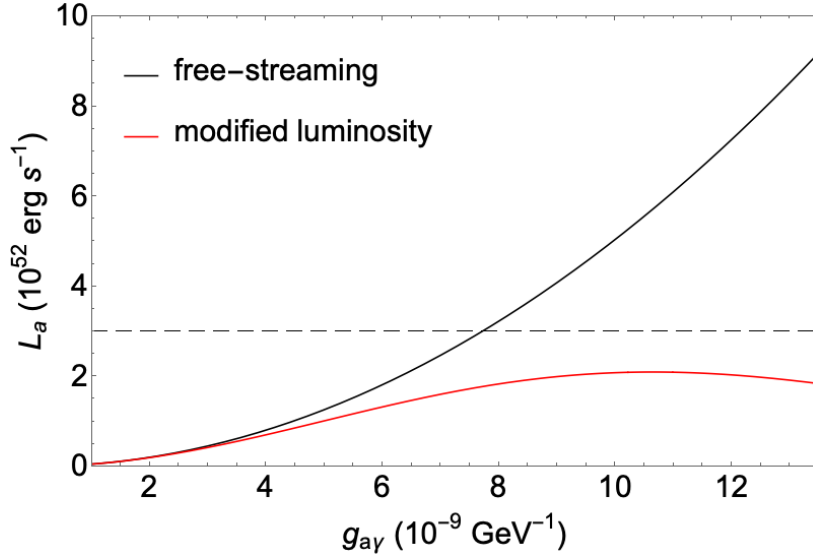


Figure 18. The ALP luminosity in the free-streaming approximation Eq. (3.7) (black line) and the modified luminosity Eq. (4.9) (red line) as a function of the coupling constant $g_{a\gamma}$ for an ALP with mass $m_a = 280$ MeV. The dashed horizontal line represent the critical value $L_\nu = 3 \times 10^{52}$ erg s $^{-1}$.

the dashed black line in Fig. 17 represents the border between the free-streaming (lower $g_{a\gamma}$) and the trapping regime (higher $g_{a\gamma}$), obtained by imposing the condition [52]

$$\tau_a(R_p, R_\nu) = \int_{R_p}^{R_\nu} dr \kappa_a \rho = 1, \quad (\text{A.7})$$

where R_p is the mean radius at which the axions are produced

$$R_p = \frac{\int dr r Q_a(r)}{\int dr Q_a(r)}. \quad (\text{A.8})$$

The condition in Eq. (A.7) corresponds to the requirement that an ALP produced at R_p should emerge from the neutrino-sphere, with a survival probability e^{-1} . The dashed line intersects the “modified luminosity bound” at the transition between the two regimes at $m_a \approx 266$ MeV, while it crosses the free-streaming bound at $m_a \approx 290$ MeV. Therefore the energy-loss argument is surely no more reliable for higher masses, which is the reason why the exclusion region has been cut with a vertical line at this value of the mass. However, the free-streaming approximation is not completely reliable for masses just below this limit too. As shown in Fig. 18, for an ALP with mass $m_a = 280$ MeV in the free-streaming approximation Eq. (3.7) values of the coupling $g_{a\gamma} \gtrsim 7.7 \times 10^{-9}$ GeV $^{-1}$ are excluded, while the modified luminosity Eq. (4.9) (which takes into account the axion decay, non-negligible for heavy ALPs) does not violate the bound for any value of the coupling constant.

While for the free-streaming the only problem is related to the validity limit of this regime, the situation for the trapping regime is more complex. In particular, in the low-mass limit ($m_a \lesssim 10$ MeV) the modified luminosity criterion allows one to exclude values of the coupling larger than those excluded by evaluating the ALP emission at the axion-sphere radius in Eq. (A.4). Indeed, the black-body bound ($g_{a\gamma} \lesssim 7.7 \times 10^{-6}$ GeV $^{-1}$) ceases because the axion-sphere moves outside from the neutrino-sphere, as shown in the upper

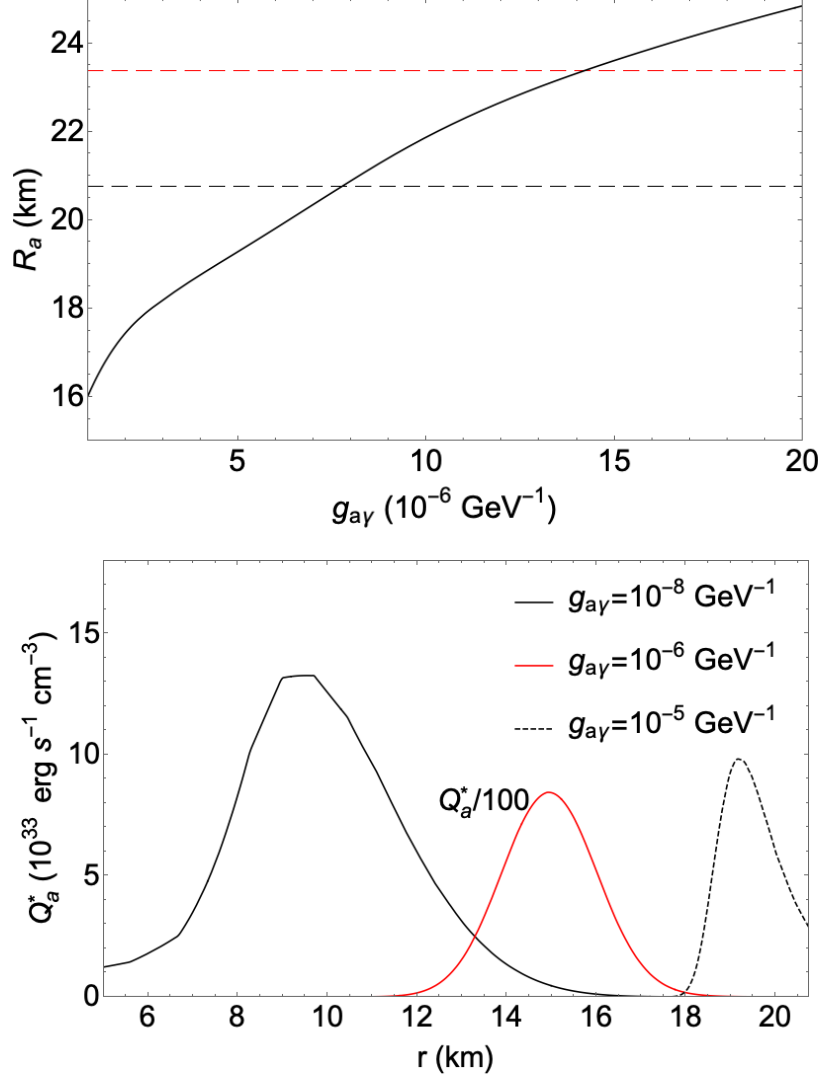


Figure 19. *Upper panel:* The axion-sphere radius R_a as a function of the coupling constant $g_{a\gamma}$ for an ALP with mass $m_a = 100$ keV. The dashed horizontal lines correspond to R_ν (black) and R_{gain} (red). *Lower panel:* The integrand in Eq. (4.9) $Q_a^* \equiv Q_a(r)e^{-\tau_a^*(r, R_{\text{far}})}$ as a function of the radius for an ALP with mass $m_a = 100$ keV and different values of $g_{a\gamma}$ as shown in legend. Notice that for $g_{a\gamma} = 10^{-6} \text{ GeV}^{-1}$ (red curve) Q_a^* has been divided by a factor 100 to be of the same order of magnitude of the other quantities in the plot.

panel of Fig. 19. On the other hand, for slightly larger values of the coupling constant, although $R_a > R_\nu$, the modified luminosity remains large enough to violate the bound. This suggests that the thermal emission underestimates the effective luminosity. In the lower panel of Fig. 19 we show the integrand in Eq. (4.9) $Q_a^* \equiv Q_a(r)e^{-\tau_a^*(r, R_{\text{far}})}$ as a function of the radius for increasing values of $g_{a\gamma}$. As the coupling constant increases, the integrand becomes narrower but it does not become a delta function, therefore the black-body emission underestimates the real luminosity since the production region is quite larger than a fixed radius typical of a thermal emission. Additionally, in the region of large mass and high coupling the bound obtained by comparing the opacities is larger than the one obtained

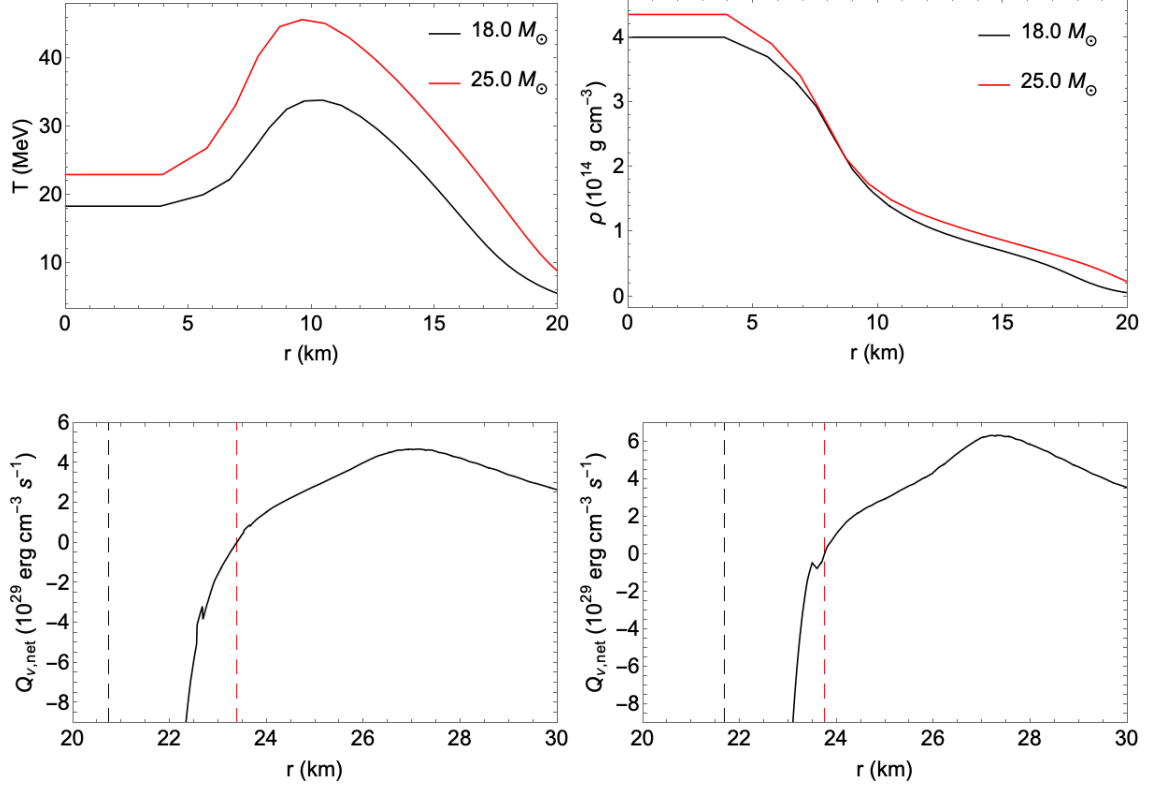


Figure 20. *Upper Left Panel:* The radial profile of the temperature T at $t_{\text{pb}} = 1$ s for the $18 M_{\odot}$ (black line) and the $25 M_{\odot}$ (red line) model. *Upper Right Panel:* The radial profile of the matter density ρ at $t_{\text{pb}} = 1$ s for the $18 M_{\odot}$ (black line) and the $25 M_{\odot}$ (red line) model. *Lower Left Panel:* The neutrino net heating rate $Q_{\nu,\text{net}}$ for the $18 M_{\odot}$ model at $t_{\text{pb}} = 1$ s. *Lower Right Panel:* The neutrino net heating rate $Q_{\nu,\text{net}}$ for the $25 M_{\odot}$ model at $t_{\text{pb}} = 1$ s. In the lower panels, the vertical dashed lines correspond to the neutrino-sphere radius (black) and the gain radius (red).

through the modified luminosity criterion. Indeed, for the latter criterion the axions have to go out from the gain radius to contribute to the energy loss. Therefore, the reason for the discrepancy in this region is that there are values of the ALP parameters for which the axion mfp is longer than that of the neutrino, hence violates the opacity comparison, but it is still shorter than $R_{\text{gain}} - R_{\nu}$, thus the axions do not go far enough to modify the neutrino signal. Since a self-consistent inclusion of ALPs in a SN simulation is necessary to show that the SN evolution actually changes if the axion mfp is larger than the neutrino one, without a SN simulation which takes into account the axions feedback the “modified luminosity criterion” is surely the most reliable strategy to constrain the ALP parameter space.

B Effect of the progenitor mass on the bound

In order to assess how the SN 1987A bound is affected by the model used, in this Section we re-evaluate it choosing a different progenitor mass. In particular, we consider a SN model with the same equations of state but a progenitor mass of $25 M_{\odot}$, larger than the one of our reference model ($18 M_{\odot}$). In Fig. 20 the radial profiles of the temperature T (upper left panel) and the matter density ρ (upper right panel) at $t_{\text{pb}} = 1$ s for the $18 M_{\odot}$ (black curves) and $25 M_{\odot}$ (red curves) models are compared. In the ALP production region

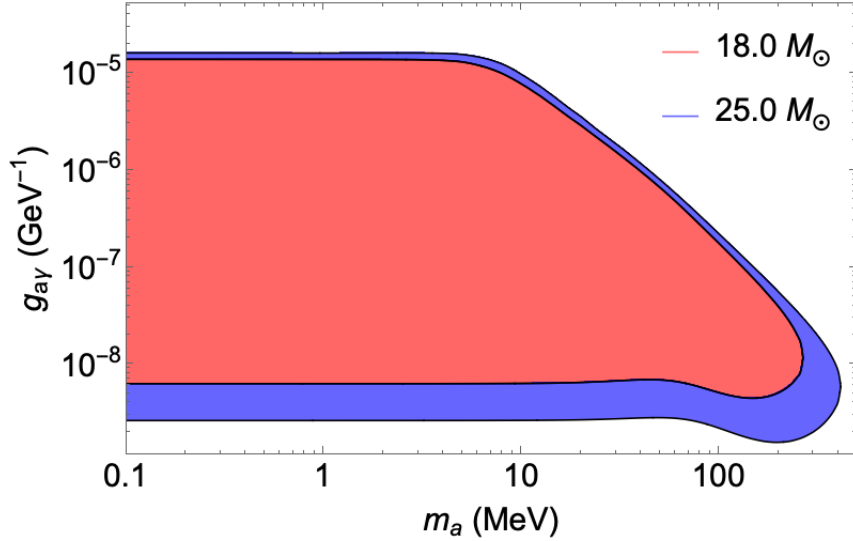


Figure 21. The ALP exclusion plot in the plane $m_a - g_{a\gamma}$ obtained through the modified luminosity criterion. The red region corresponds to the exclusion plot for a $18 M_{\odot}$ case, while the blue one refers to $25 M_{\odot}$.

($5 \text{ km} \lesssim r \lesssim 15 \text{ km}$) the temperature is about 10 MeV larger in the $25 M_{\odot}$ model, while the matter density does not change very much. In order to compute the “modified luminosity” in Eq. (4.2) at $t_{\text{pb}} = 1 \text{ s}$, we assume the core radius $R_c = 10 \text{ km}$, while by using the same approach described in Sec. 2.4 the neutrino-sphere radius and the gain radius result to be respectively $R_{\nu} = 21.7 \text{ km}$ and $R_{\text{gain}} = 23.7 \text{ km}$ for the $25 M_{\odot}$ model, slightly larger than the corresponding quantities in the reference model, as shown in the lower panels of Fig. 20. In Fig. 21 we show how the bound changes with the SN model. It is apparent that through the $25 M_{\odot}$ model the exclusion region is larger than the one excluded with the $18 M_{\odot}$ model. In particular, the discrepancy in the free-streaming regime is more substantial than the one in the trapping regime. Indeed, the core temperature of the star increases substantially when moving to larger progenitor masses. Since the axion production rate is a steep function of the temperature, in the free-streaming regime the energy loss in ALPs is much larger and thus the bound is stronger. On the other hand, in the trapping regime the bound does not change very much. In this regime the bound depends on the difference $R_{\text{gain}} - R_{\nu}$ which slightly increases with the progenitor mass. Therefore the bound in the trapping regime is slightly stronger for larger progenitor mass. Naively, the same results can be obtained also with the “black-body approximation”. Since axions thermalize in the trapping regime, the luminosity depends only on the temperature of the surface emission and a lot of information about the star is lost, therefore the bound is not very sensitive to the SN model.

References

- [1] L. Di Luzio, M. Giannotti, E. Nardi and L. Visinelli, “The landscape of QCD axion models,” [arXiv:2003.01100 [hep-ph]].
- [2] P. Svrcek and E. Witten, “Axions In String Theory,” JHEP **0606**, 051 (2006) doi:10.1088/1126-6708/2006/06/051 [hep-th/0605206].

- [3] A. Arvanitaki, S. Dimopoulos, S. Dubovsky, N. Kaloper and J. March-Russell, “String Axiverse,” *Phys. Rev. D* **81**, 123530 (2010) doi:10.1103/PhysRevD.81.123530 [arXiv:0905.4720 [hep-th]].
- [4] M. Cicoli, M. Goodsell and A. Ringwald, “The type IIB string axiverse and its low-energy phenomenology,” *JHEP* **1210**, 146 (2012) doi:10.1007/JHEP10(2012)146 [arXiv:1206.0819 [hep-th]].
- [5] P. W. Graham, D. E. Kaplan and S. Rajendran, “Cosmological Relaxation of the Electroweak Scale,” *Phys. Rev. Lett.* **115**, no. 22, 221801 (2015) doi:10.1103/PhysRevLett.115.221801 [arXiv:1504.07551 [hep-ph]].
- [6] Y. Hochberg, E. Kuflik, R. McGehee, H. Murayama and K. Schutz, “Strongly interacting massive particles through the axion portal,” *Phys. Rev. D* **98**, no. 11, 115031 (2018) doi:10.1103/PhysRevD.98.115031 [arXiv:1806.10139 [hep-ph]].
- [7] C. Boehm, M. J. Dolan, C. McCabe, M. Spannowsky and C. J. Wallace, *JCAP* **1405**, 009 (2014) doi:10.1088/1475-7516/2014/05/009 [arXiv:1401.6458 [hep-ph]].
- [8] M. J. Dolan, T. Ferber, C. Hearty, F. Kahlhoefer and K. Schmidt-Hoberg, “Revised constraints and Belle II sensitivity for visible and invisible axion-like particles,” *JHEP* **1712**, 094 (2017) doi:10.1007/JHEP12(2017)094 [arXiv:1709.00009 [hep-ph]].
- [9] D. Cadamuro, S. Hannestad, G. Raffelt and J. Redondo, “Cosmological bounds on sub-MeV mass axions,” *JCAP* **1102**, 003 (2011) doi:10.1088/1475-7516/2011/02/003 [arXiv:1011.3694 [hep-ph]].
- [10] D. Cadamuro and J. Redondo, “Cosmological bounds on pseudo Nambu-Goldstone bosons,” *JCAP* **1202**, 032 (2012) doi:10.1088/1475-7516/2012/02/032 [arXiv:1110.2895 [hep-ph]].
- [11] P. F. Depta, M. Hufnagel and K. Schmidt-Hoberg, “Robust cosmological constraints on axion-like particles,” arXiv:2002.08370 [hep-ph].
- [12] P. Carena, O. Straniero, B. Döbrich, M. Giannotti, G. Lucente and A. Mirizzi, “Constraints on the coupling with photons of heavy axion-like-particles from Globular Clusters,” arXiv:2004.08399 [hep-ph].
- [13] J. Jaeckel and M. Spannowsky, “Probing MeV to 90 GeV axion-like particles with LEP and LHC,” *Phys. Lett. B* **753**, 482 (2016) doi:10.1016/j.physletb.2015.12.037 [arXiv:1509.00476 [hep-ph]].
- [14] B. Döbrich, J. Jaeckel and T. Spadaro, “Light in the beam dump. Axion-Like Particle production from decay photons in proton beam-dumps,” *JHEP* **1905**, 213 (2019) doi:10.1007/JHEP05(2019)213 [arXiv:1904.02091 [hep-ph]].
- [15] D. Banerjee *et al.* [NA64], “Search for Axionlike and Scalar Particles with the NA64 Experiment,” *Phys. Rev. Lett.* **125**, no.8, 081801 (2020) doi:10.1103/PhysRevLett.125.081801 [arXiv:2005.02710 [hep-ex]].
- [16] J. W. Brockway, E. D. Carlson and G. G. Raffelt, “SN1987A gamma-ray limits on the conversion of pseudoscalars,” *Phys. Lett. B* **383**, 439-443 (1996) doi:10.1016/0370-2693(96)00778-2 [arXiv:astro-ph/9605197 [astro-ph]].
- [17] J. Grifols, E. Masso and R. Toldra, “Gamma-rays from SN1987A due to pseudoscalar conversion,” *Phys. Rev. Lett.* **77**, 2372-2375 (1996) doi:10.1103/PhysRevLett.77.2372 [arXiv:astro-ph/9606028 [astro-ph]].
- [18] A. Payez, C. Evoli, T. Fischer, M. Giannotti, A. Mirizzi and A. Ringwald, “Revisiting the SN1987A gamma-ray limit on ultralight axion-like particles,” *JCAP* **02**, 006 (2015) doi:10.1088/1475-7516/2015/02/006 [arXiv:1410.3747 [astro-ph.HE]].
- [19] E. Masso and R. Toldra, “On a light spinless particle coupled to photons,” *Phys. Rev. D* **52**, 1755-1763 (1995) doi:10.1103/PhysRevD.52.1755 [arXiv:hep-ph/9503293 [hep-ph]].

- [20] J. S. Lee, “Revisiting Supernova 1987A Limits on Axion-Like-Particles,” [arXiv:1808.10136 [hep-ph]].
- [21] M. Giannotti, L. Duffy and R. Nita, “New constraints for heavy axion-like particles from supernovae,” *JCAP* **01**, 015 (2011) doi:10.1088/1475-7516/2011/01/015 [arXiv:1009.5714 [astro-ph.HE]].
- [22] J. Jaeckel, P. Malta and J. Redondo, “Decay photons from the axionlike particles burst of type II supernovae,” *Phys. Rev. D* **98**, no.5, 055032 (2018) doi:10.1103/PhysRevD.98.055032 [arXiv:1702.02964 [hep-ph]].
- [23] A. Mezzacappa and S. W. Bruenn, “A numerical method for solving the neutrino Boltzmann equation coupled to spherically symmetric stellar core collapse,” *Astrophys. J.* **405**, 669 (1993). doi:10.1086/172395
- [24] M. Liebendoerfer, O. E. B. Messer, A. Mezzacappa, S. W. Bruenn, C. Y. Cardall and F. K. Thielemann, “A Finite difference representation of neutrino radiation hydrodynamics for spherically symmetric general relativistic supernova simulations,” *Astrophys. J. Suppl.* **150**, 263 (2004) doi:10.1086/380191 [astro-ph/0207036].
- [25] T. Fischer, G. Guo, A. A. Dzhioev, G. Martínez-Pinedo, M. R. Wu, A. Lohs and Y. Z. Qian, “Neutrino signal from proto-neutron star evolution: Effects of opacities from charged-current–neutrino interactions and inverse neutron decay,” *Phys. Rev. C* **101**, no.2, 025804 (2020) doi:10.1103/PhysRevC.101.025804 [arXiv:1804.10890 [astro-ph.HE]].
- [26] S. E. Woosley, A. Heger and T. A. Weaver, “The evolution and explosion of massive stars”, *Rev. Mod. Phys.* **74**, 1015 (2002) doi:10.1103/RevModPhys.74.1015
- [27] K. Nomoto “Evolution of 8-10 solar mass stars toward electron capture supernovae. I - Formation of electron-degenerate O + NE + MG cores.” *Astrophys. J.* **277**, 791 (1984) doi:10.1086/161749
- [28] S. Jones, R. Hirschi, K. Nomoto, et al. “Advanced Burning Stages and Fate of 8-10 M_{\odot} Stars,” *Astrophys. J.* **772**, 150 (2013) doi:10.1088/0004-637X/772/2/150
- [29] L. Hudepohl, B. Muller, H. T. Janka, A. Marek and G. Raffelt, “Neutrino Signal of Electron-Capture Supernovae from Core Collapse to Cooling,” *Phys. Rev. Lett.* **104**, 251101 (2010) doi:10.1103/PhysRevLett.104.251101 [arXiv:0912.0260 [astro-ph.SR]].
- [30] T. Fischer, S. Whitehouse, A. Mezzacappa, F. K. Thielemann and M. Liebendorfer, “Protoneutron star evolution and the neutrino driven wind in general relativistic neutrino radiation hydrodynamics simulations,” *Astron. Astrophys.* **517**, A80 (2010) doi:10.1051/0004-6361/200913106 [arXiv:0908.1871 [astro-ph.HE]].
- [31] A. Kopf and G. Raffelt, “Photon dispersion in a supernova core,” *Phys. Rev. D* **57** (1998) 3235 doi:10.1103/PhysRevD.57.3235 [astro-ph/9711196].
- [32] M. Hempel and J. Schaffner-Bielich, “Statistical Model for a Complete Supernova Equation of State,” *Nucl. Phys. A* **837**, 210 (2010) doi:10.1016/j.nuclphysa.2010.02.010 [arXiv:0911.4073 [nucl-th]].
- [33] M. Hempel, T. Fischer, J. Schaffner-Bielich and M. Liebendorfer, “New Equations of State in Simulations of Core-Collapse Supernovae,” *Astrophys. J.* **748**, 70 (2012) doi:10.1088/0004-637X/748/1/70 [arXiv:1108.0848 [astro-ph.HE]].
- [34] M. Hempel, “Nucleon self-energies for supernova equations of state,” *Phys. Rev. C* **91**, 055807 (2015) doi:10.1103/PhysRevC.91.055807 [arXiv:1410.6337 [nucl-th]].
- [35] T. Fischer, M. Hempel, I. Sagert, Y. Suwa and J. Schaffner-Bielich, “Symmetry energy impact in simulations of core-collapse supernovae” *European Physical Journal* **A50**, 46 (2014) doi:10.1140/epja/i2014-14046-5

- [36] T. Fischer, G. Martínez-Pinedo, M. Hempel, and M. Liebendörfer, “Neutrino spectra evolution during protoneutron star deleptonization,” *Phys. Rev.* **D85**, 083003 (2012) doi:10.1103/PhysRevD.85.083003
- [37] H. T. Janka, “Conditions for shock revival by neutrino heating in core collapse supernovae,” *Astron. Astrophys.* **368**, 527 (2001) doi:10.1051/0004-6361:20010012 [arXiv:astro-ph/0008432 [astro-ph]].
- [38] T. Fischer, “The role of medium modifications for neutrino-pair processes from nucleon-nucleon bremsstrahlung - Impact on the protoneutron star deleptonization,” *Astron. Astrophys.* **593**, A103 (2016) doi:10.1051/0004-6361/201628991 [arXiv:1608.05004 [astro-ph.HE]].
- [39] G. Raffelt and L. Stodolsky, “Mixing of the Photon with Low Mass Particles,” *Phys. Rev. D* **37**, 1237 (1988) doi:10.1103/PhysRevD.37.1237
- [40] L. Di Lella, A. Pilaftsis, G. Raffelt and K. Zioutas, “Search for solar Kaluza-Klein axions in theories of low scale quantum gravity,” *Phys. Rev. D* **62**, 125011 (2000) doi:10.1103/PhysRevD.62.125011 [arXiv:hep-ph/0006327 [hep-ph]].
- [41] G. Pagliaroli, F. Vissani, M. Costantini and A. Ianni, “Improved analysis of SN1987A antineutrino events,” *Astropart. Phys.* **31**, 163-176 (2009) doi:10.1016/j.astropartphys.2008.12.010 [arXiv:0810.0466 [astro-ph]].
- [42] G. G. Raffelt, “Astrophysical axion bounds,” *Lect. Notes Phys.* **741**, 51-71 (2008) doi:10.1007/978-3-540-73518-2_3 [arXiv:hep-ph/0611350 [hep-ph]].
- [43] J. H. Chang, R. Essig and S. D. McDermott, “Revisiting Supernova 1987A Constraints on Dark Photons,” *JHEP* **01**, 107 (2017) doi:10.1007/JHEP01(2017)107 [arXiv:1611.03864 [hep-ph]].
- [44] F. Ertas and F. Kahlhoefer, “On the interplay between astrophysical and laboratory probes of MeV-scale axion-like particles,” [arXiv:2004.01193 [hep-ph]].
- [45] H. Dreiner, C. Hanhart, U. Langenfeld and D. R. Phillips, “Supernovae and light neutralinos: SN1987A bounds on supersymmetry revisited,” *Phys. Rev. D* **68**, 055004 (2003) doi:10.1103/PhysRevD.68.055004 [arXiv:hep-ph/0304289 [hep-ph]].
- [46] W. DeRocco and P. W. Graham, “Constraining Primordial Black Hole Abundance with the Galactic 511 keV Line,” *Phys. Rev. Lett.* **123**, no.25, 251102 (2019) doi:10.1103/PhysRevLett.123.251102 [arXiv:1906.07740 [astro-ph.CO]].
- [47] B. Müller, T. Melson, A. Heger and H. T. Janka, “Supernova simulations from a 3D progenitor model – Impact of perturbations and evolution of explosion properties,” *Mon. Not. Roy. Astron. Soc.* **472**, no.1, 491-513 (2017) doi:10.1093/mnras/stx1962 [arXiv:1705.00620 [astro-ph.SR]].
- [48] G. M. Fuller, A. Kusenko and K. Petraki, “Heavy sterile neutrinos and supernova explosions,” *Phys. Lett. B* **670**, 281-284 (2009) doi:10.1016/j.physletb.2008.11.016 [arXiv:0806.4273 [astro-ph]].
- [49] A. Sung, H. Tu and M. R. Wu, “New constraint from supernova explosions on light particles beyond the Standard Model,” *Phys. Rev. D* **99**, no.12, 121305 (2019) doi:10.1103/PhysRevD.99.121305 [arXiv:1903.07923 [hep-ph]].
- [50] D. N. Schramm and J. R. Wilson, “SUPERNOVAE INDUCED BY AXION LIKE PARTICLES,” *Astrophys. J.* **260**, 868 (1982) doi:10.1086/160305
- [51] T. Rembiasz, M. Obergaulinger, M. Masip, M. Á. Pérez-García, M. Á. Aloy and C. Albertus, “Heavy sterile neutrinos in stellar core-collapse,” *Phys. Rev. D* **98**, no.10, 103010 (2018) doi:10.1103/PhysRevD.98.103010 [arXiv:1806.03300 [astro-ph.HE]].
- [52] G. G. Raffelt, “Stars as laboratories for fundamental physics : The astrophysics of neutrinos, axions, and other weakly interacting particles,” Chicago, USA: Univ. Pr. (1996) 664 p.

- [53] G. Raffelt and D. Seckel, “Bounds on Exotic Particle Interactions from SN 1987a,” *Phys. Rev. Lett.* **60**, 1793 (1988) doi:10.1103/PhysRevLett.60.1793